Prematurity Reprograms Cerebellar Development and Long-Term Behavior

Georgios Sanidas[1,2 **], Gabriele Simonti[1,2**], Javid Ghaemmaghami[3], Kyla Woyshner[4], Nora Wolff[1,2], Chad Byrd[1,2], Maria Triantafyllou[1,2], Courtney Lowe[1], Henry Salisbury[5], Evan Goldstein[6], Aaron Sathyanesan[5], Robinson Vidva[1], Ioannis Koutroulis[1,2], Genevieve Stein-O'Brien[4], Dimitrios N Sidiropoulos[4], Vittorio Gallo[7,8*] and Panagiotis Kratimenos[1,2*]

[1]Children's National Research Institute, Children's National Hospital, Washington, DC, USA
[2]Department of Pediatrics, The George Washington University School of Medicine and Health Sciences, Washington, DC, USA
[3] Department of Computational Medicine & Bioinformatics, University of Michigan, AA, USA
[4]Johns Hopkins University School of Medicine, Baltimore, MD, USA
[5]University of Dayton, Dayton, OH, USA
[6] Departments of Biological Sciences and Neuroscience & Regenerative Medicine, Augusta University, GA, USA
[7] Seattle Children's Research Institute, Seattle, WA, USA
[8] Department of Pediatrics, University of Washington School of Medicine, Seattle, WA, USA

**Equal contribution
*Corresponding Authors:
Panagiotis Kratimenos, MD, PhD
Children's National Hospital
George Washington University School of Medicine
pankratimenos@gwu.edu

Vittorio Gallo, PhD
Seattle Children's
University of Washington School of Medicine
vittorio.gallo@seattlechildrens.org

Lead contact:
Panagiotis Kratimenos, MD, PhD
Children's National Hospital
George Washington University School of Medicine
pankratimenos@gwu.edu

Abstract

Premature survivors are at risk for motor and socio-cognitive impairments, implicating cerebellar dysfunction. However, underlying mechanisms remain unclear due to the heterogeneity of preterm insults, the most prominent being prenatal maternal immune activation (MIA) and neonatal hypoxia (Hx). To examine how individual or sequential insults affect cerebellar function, we utilized a double-hit (DH) mouse model that integrates both exposures. Comparative analysis showed that this model recapitulates key features of the human preterm cerebellum, allowing systematic evaluation of insult-specific outcomes. Isolated Hx triggered S-phase arrest in mature granule cells, disrupted Purkinje cell synaptic integration, and led to both motor and social deficits. In contrast, when Hx followed MIA (DH), it delayed granule cell maturation with G2-phase retention and triggered progressive mitochondrial dysfunction. While DH mice developed motor-cognitive impairments, sociability was preserved. These findings underscore the multiplicity of neurodevelopmental outcomes in prematurity, shaped by timing and interaction of early-life insults.

Keywords: Maternal immune activation, hypoxia, cerebellum, ASD, human, locomotor, social, behavior, spatial transcriptomics.

65 **Introduction**

66 Despite significant strides in neonatal critical care that have improved survival rates for
67 extremely preterm infants (22-24 weeks gestation) [1,2,3], their neurocognitive outcome
68 improvement has plateaued in recent years[4,2]. Preterm birth exposes the developing brain to a
69 convergence of perinatal insults that disrupt key neurodevelopmental processes [4]. Maternal
70 immune activation (MIA), a key driver of spontaneous preterm labor, often results from sterile
71 intra-amniotic inflammation[4]. Implicated in approximately 40% of preterm birth cases linked to
72 intrauterine infection or inflammation[5], MIA disrupts the delicate immune tolerance required for
73 maintaining pregnancy[4,5,6], thereby triggering premature labor[4,5]. Beyond their direct role in
74 triggering labor, the immune-mediated mechanisms underlying preterm birth have profound
75 implications for fetal brain development, disrupting key processes such as neurogenesis,
76 neuronal migration, and synaptogenesis[7,8]. These disruptions increase susceptibility to
77 subsequent socio-emotional and cognitive impairments[9,10,11].

78

79 This is especially critical in preterm newborns, who face additional risks like hypoxia from
80 immature respiratory control and underdeveloped lungs, resulting in prolonged need for
81 ventilatory support[12]. Hypoxia during early postnatal period also disrupts neurodevelopmental
82 processes, such as neuronal differentiation, synaptogenesis, and myelination, and is strongly
83 linked to long-term behavioral deficits[13]. However, the sequential interaction between MIA and
84 hypoxia remains poorly understood. Clarifying how MIA-induced inflammation and hypoxia
85 interplay is essential to uncover mechanisms behind long-term neurodevelopmental deficits in
86 preterm infants.

87 Perinatal insults are major drivers of long-term neurological morbidity[14]. Affected individuals

88 often exhibit social deficits and motor impairments, including ataxia - indicating cerebellar
89 dysfunction[2,15]. The cerebellum's rapid transition to the ex-utero environment during a critical
90 window of maturation renders it especially vulnerable to hypoxic and inflammatory challenges,
91 which can disrupt both its structural integrity and functional development. Nonetheless, the
92 precise mechanisms underlying these disruptions remain incompletely understood.
93
94 We hypothesize that cerebellar structural and functional alterations extend beyond basic motor
95 control, given the cerebellum's crucial role in adaptive motor learning[16,17]. We propose that
96 primary motor deficits caused by cerebellar disruption indirectly lead to social behavior
97 impairments by limiting opportunities for peer interaction, exploration, and complex social
98 play—foundational elements of normal social development[18,19]. Emerging evidence links
99 cerebellar dysfunction to autism spectrum disorder (ASD) and emotional dysregulation[12, 20].
100 However, the mechanistic interplay between perinatal insults and cerebellar disruption in shaping
101 long-term behavioral outcomes remains unclear[21, 22]. While we previously demonstrated that
102 neonatal Hx alone disrupts cerebellar development and alters locomotion[23], the sequential impact
103 of MIA followed by Hx on cerebellar development remains unexplored. Since MIA precedes
104 preterm birth, it may prime the developing brain for increased vulnerability to postnatal Hx,
105 thereby exacerbating cerebellar dysfunction
106
107 To address these questions, we used a double-hit (DH) murine model of preterm encephalopathy
108 to dissect the independent and sequential effects of MIA and Hx on cerebellar development.
109 Grounded in comprehensive behavioral profiling, this approach aimed to define how these
110 insults impact locomotor learning and coordination. To establish the translational relevance of

111 our model, we performed comparative analyses with human preterm postmortem cerebellum,
112 evaluating the extent to which the DH paradigm recapitulates conserved cellular and molecular
113 signatures of injury across species.
114
115 To investigate how MIA and Hx disrupt cerebellar circuit formation, we applied spatial
116 transcriptomics within the anatomical context of the developing cerebellum, capturing molecular
117 profiles linked to cytoarchitectural changes during postnatal maturation. This approach allowed
118 us to define how each insult alters transcriptional programs governing progenitor differentiation,
119 laminar organization, and circuit assembly. We complemented this analysis with histological
120 evaluation and cell cycle mapping to delineate insult-specific effects on progenitor maturation
121 across cerebellar cortical layers. Finally, we assessed how locomotor dysfunction influences
122 social behavior by combining social behavioral analysis with detailed kinematic analysis to
123 dissect cerebellar contributions to socio-cognitive phenotypes.
124
125 Through this integrative approach, we aimed to uncover how fetal exposure to immune
126 activation and hypoxia disrupts cerebellar architecture and connectivity. We hypothesized that
127 these disruptions impair circuit formation across development, resulting in motor learning
128 deficits and altered social behavior, thereby providing critical insight into the pathogenesis of
129 neurodevelopmental disorders in preterm populations.
130
131
132

Results

A Double-Hit Mouse Model of Perinatal Brain Injury

To delineate the individual and sequential effects of preterm-associated insults on long-term neurobehavioral outcomes, we utilized the DH mouse model. This model replicates two common insults experienced by human preterm neonates: prenatal MIA, simulating events during or preceding preterm labor, followed by sustained postnatal Hx, representing the consequences of pulmonary immaturity and the associated need for respiratory support. A key challenge in modeling human prematurity in mice is the significant difference in their gestational timelines and developmental trajectories. A full-term mouse pregnancy lasts approximately 19-21 days, producing a pup developmentally comparable to a late preterm or near-term human infant[24]. Consequently, inducing birth even one day early in a mouse is analogous to extreme human prematurity (<28 weeks of gestation)[25]. Therefore, we modeled MIA in pregnant dams by intraperitoneally injecting lipopolysaccharide (LPS) on embryonic days 15 and 16 (E15/E16), while control dams received normal saline (**Fig. 1a).** This time point was selected because it consistently triggers preterm delivery at E18-E19, a developmental stage that corresponds to approximately 22–24 weeks of human gestation based on Theiler staging and other cross-species developmental frameworks [26,27,28]. (**Fig. 1a)**. To model postnatal hypoxic conditions, we employed a well-established paradigm of sublethal neonatal Hx previously validated by our group and others[29,30,31,30]. From postnatal day 3 (P3) to P11, pups were housed in a hypoxic chamber while littermate controls were maintained under standard normoxic (N) conditions. This design resulted in four experimental groups: a control group (Sal-N), two single-insult groups (MIA alone; LPS-N and Hx alone; Sal-Hx), and the double-hit group (DH; LPS-Hx).

156 *MIA Exacerbates Hx-induced Long-term Cerebellar Functional Deficits*

157 Preterm born children often exhibit elevated ataxia scores, reflecting of long-term impairments in
158 coordination and balance linked to cerebellar dysfunction[20]. To assess cerebellar-dependent
159 motor function following perinatal insults, we employed the ErasmusLadder, a high-precision
160 tool designed to evaluate cerebellar-mediated gait patterns and motor learning[13,32,33,34]. The
161 ErasmusLadder is a motorized apparatus with horizontal, touch-sensitive rungs that detect the
162 timing and position of each step taken by a mouse. To evaluate motor learning and adaptive
163 locomotion, the system automatically introduces obstacles, prompting the mouse to adjust its
164 stepping strategy in response to these perturbations. This system is highly sensitive to subtle
165 impairments in baseline locomotion, sensorimotor adaptation, and associative motor learning,
166 making it ideally suited for detecting cerebellar-related abnormalities[35] **(Fig. 1b-c)**.
167
168 We first assessed higher motor-cognitive functions by evaluating the locomotor response to
169 obstacle presentation. Locomotor learning and adaptability were impaired in all experimental
170 groups (LPS-N, Sal-Hx, and DH) compared to controls. However, the DH group showed the
171 most severe impairments, with an approximately twofold increase in post-perturbation step time
172 compared to controls, indicating markedly delayed adaptive responses to both obstacles and
173 auditory cues **(Fig. 1d and Extended Data Fig. 1a)**. These findings suggest that while MIA and
174 Hx each independently impair motor learning and response, their sequential occurrence in DH
175 mice synergistically worsens deficits in cerebellar-mediated sensorimotor plasticity.
176
177 Next, we assessed coordination and balance parameters. Locomotor missteps were primarily
178 influenced by Hx exposure. Mice in the Sal-Hx group exhibited a 10% increase in missteps

179 compared to other groups, indicating impaired motor coordination. In contrast, MIA-exposed
180 groups (LPS-N, DH) did not show significant differences in misstep frequency **(Fig. 1e and**
181 **Extended Data Fig. 1b)**.
182
183 Collectively, these findings suggest that prenatal MIA and neonatal Hx each disrupt cerebellar-
184 dependent motor processes, though their sequential occurrence results in distinct and more
185 severe outcomes. Hx exposure primarily impaired coordination and was also linked to deficits in
186 motor adaptability and learning. In contrast, consecutive exposure to MIA and Hx in the DH
187 group led to the most profound impairments in sensorimotor integration, underscoring the
188 synergistic and additive impact of sequential prenatal and postnatal insults on cerebellar-
189 regulated functions.
190
191 *MIA and Hx Reproduce Structural Features of the Preterm Human Cerebellum*
192 To identify the cellular pathologies underlying the observed deficits in motor learning and
193 coordination, we conducted a neuroanatomical analysis of the mouse cerebellum at postnatal
194 days 11 (P11) and 45 (P45). At P11, all insult groups exhibited structural cerebellar alterations,
195 highlighting an early vulnerability to both isolated and consecutive combined insults.
196 Specifically, Purkinje cell (PC) counts were significantly reduced in the LPS-N and DH groups
197 **(Fig. 2a-b)**. Granule cell (GC) abnormalities were also observed: the LPS-N and DH groups
198 showed an expanded external granule layer (EGL), while the Sal-Hx and DH groups exhibited a
199 decreased density in the mature internal granular layer (IGL) **(Fig. 2h-i)**. These findings suggest
200 that sequential MIA and Hx exposure impairs GC maturation across the cerebellar cortical
201 layers.

By P45, the cerebellar alterations became more distinct between groups, revealing divergent and long-term effects of each insult. The LPS-N and DH groups showed the most pronounced morphological PC injury, characterized with cellular shrinkage, poorly defined nuclei, and perineuronal vacuolization **(Fig. 2c-g)**. These structural changes extended beyond individual cell bodies, presenting as neuropil rarefaction **(Fig. 2a-f)**, which indicates disrupted connectivity. This finding was further supported by a reduction in the length and complexity of PC dendritic arborization, despite PC counts normalizing by adulthood **(Fig. 2c-f).** In contrast, hypoxia alone (Sal-Hx) primarily reduced mature GC density in the IGL by adulthood—an effect also observed in the DH groups **(Fig. 2h-j)**.

Building on the cerebellar abnormalities identified in the DH mouse model, we next assessed its translational relevance by examining similar structural changes in human preterm cerebellar tissue. We conducted a comparative analysis of postmortem cerebellar samples from preterm and term infants (**Tables 1 and 2**) to evaluate the impact of preterm birth on cerebellar cytoarchitecture. Preterm cerebella displayed pronounced abnormalities across cortical layers, including disrupted GC distribution and maturation, closely resembling those observed in the DH mouse (**Fig. 2l–q**).

While individual insults produced distinct effects - Hx primarily impacting mature GCs and MIA compromising PC integrity and impairing granule cell precursor (GCP) maturation - the consecutive exposure in DH mice resulted in a cellular phenotype closely resembling that of the human preterm cerebellum. This convergence likely reflects the clinical progression in which

225 prenatal immune activation is followed by postnatal hypoxic events in preterm infants.
226 Therefore, the structural parallels between DH mice and human preterm cerebella support the
227 translational validity of the DH model in capturing the compounded impact of consecutive
228 perinatal insults on cerebellar development.
229
230 *MIA Reconfigures the Cerebellar Response to Hx*
231 Given the shared behavioral and cerebellar cellular phenotypes between our model and human
232 preterm infants, we next explored the molecular basis of the insult-specific cellular alterations.
233 Comparative transcriptomic analysis contrasting the DH mouse model at P11 with human
234 cerebellar tissue (preterm versus term; **Table 1-2)** revealed that a substantial subset of
235 differential expressed genes (DEGs) in the mouse insult groups exhibited corresponding
236 differential expression in human preterm samples **(Extended Data Fig. 2-1a)**.
237 Functional enrichment of the shared DEGs demonstrated convergence on biological processes
238 critical for cerebellar development, including axonogenesis, neuronal differentiation,
239 neurotransmitter signaling, and extracellular matrix remodeling **(Extended Data Fig. 2-1)**—
240 with the latter likely reflecting postmortem tissue effects in human samples[36]. Each comparison
241 highlights how distinct perinatal insults - whether isolated or sequential - differentially influence
242 cerebellar development at the molecular level. The observed overlap in gene expression between
243 each modeled insult and the human preterm cerebellum supports the view that preterm
244 cerebellopathy is not a uniform condition, but rather a spectrum of injury patterns shaped by
245 diverse clinical trajectories. These findings further establish the DH mouse model as a
246 translationally relevant in vivo platform for dissecting the molecular mechanisms underlying

247 human preterm cerebellar injury, highlighting how the type and sequence of perinatal insults
248 shape distinct molecular trajectories with potential long-term developmental consequences.
249
250 Having validated the relevance of the DH model to the human preterm cerebellum transcriptome,
251 we next leveraged this platform to dissect the molecular signatures associated with each perinatal
252 insult. We performed transcriptomic profiling at P11 and P45 to capture both the acute response
253 to Hx and the long-term molecular adaptations underlying recovery from late childhood into
254 adulthood. Given that the cellular analyses identified mature GCs as the primary targets of Hx,
255 we examined the transcriptional response to Hx at P11. Hx alone resulted in a striking 12,508
256 DEGs **(Extended Data Fig. 2-2a)**. Pathway enrichment analysis revealed disruptions in protein
257 metabolism and mitochondrial organization **(Extended Data Fig. 2-3a)**. By P45, the
258 transcriptomic landscape in Sal-Hx mice had shifted, showing enrichment in pathways related to
259 axonogenesis and membrane potential regulation - suggesting ongoing circuit-level
260 reorganization **(Extended Data Fig. 2-3c)**. In contrast, MIA alone did not elicit significant
261 transcriptional changes at P11. However, by P45, MIA-exposed mice displayed molecular
262 alterations resembling those observed in Sal-Hx mice, along with additional transcriptional
263 signatures related to cognition and learning **(Extended Data Fig. 2-2b-c)**. These findings
264 highlight distinct temporal patterns in the transcriptional response to Hx and MIA: whereas Hx
265 induces early molecular changes, MIA triggers a delayed transcriptomic reprogramming that
266 may gradually influence cognitive function later in development.
267
268 Given the sequential nature of perinatal insults in prematurity, we investigated how prior MIA
269 exposure modulates the cerebellar response to Hx by comparing the DH and Sal-Hx groups. At

270 P11, the DH group showed significant upregulation of genes involved in mitochondrial
271 respiration compared to Sal-Hx alone, with pathway enrichment in mitochondrial metabolism,
272 oxidative phosphorylation, and ATP synthesis **(Extended Data Fig. 2-3b)**. These results suggest
273 that MIA primes the cerebellum for an amplified metabolic response to hypoxic stress. By P45,
274 however, DH mice exhibited distinct transcriptional profiles, marked by alterations in pathways
275 related to synaptogenesis, cognition, learning, and locomotor behavior – changes not observed in
276 the Sal-Hx group alone **(Extended Data Fig. 2-3d)**.
277
278 These findings highlight that MIA modifies both the immediate and long-term molecular
279 consequences of neonatal Hx, leading to persistent alterations in cerebellar energy metabolism,
280 as well as changes in synaptic function and behavior. Together, these disruptions may contribute
281 to the locomotor deficit observed in DH mice.
282
283 *Spatial Transcriptomics Reveal Insult-Specific Disruption of Cerebellar Developmental*
284 *Programs*
285 To examine how each perinatal insult influences the transcriptional programs underlying circuit
286 assembly and cytoarchitectural organization in the developing cerebellum, we performed spatial
287 transcriptomics (Visium) on postnatal cerebellar tissue **(Fig. 3a)**. Using CoGAPS – an
288 unsupervised analysis framework for coordinated gene activity in patterned sets – we identified
289 13 biologically meaningful transcriptional patterns (M-patterns), each localized to specific
290 cerebellar cortical layers and cell types **(Fig. 3a-c)**. Gene set enrichment analysis of the high-
291 amplitude genes driving these M-patterns revealed significant associations with distinct
292 biological processes and cell-type-markers **(Fig. 3e).**

293

294 To determine how each perinatal insult alters spatial gene expression in the cerebellum, we
295 evaluated M-pattern enrichment across experimental groups. In control (Sal-N) mice, M-pattern
296 11 (M11) showed a strong positive correlation, reflecting the baseline spatial transcriptional
297 architecture of the postnatal cerebellum **(Fig. 3c)**. M11, which was not restricted to PCs or GCs
298 **(Fig. 3b)**, was enriched for pathways related to protein synthesis, translation, and oxidative
299 phosphorylation **(Supplemental files)**. In contrast, M11 exhibited a negative correlation across
300 all insult-exposed groups **(Fig. 3c)**, indicating a common disruption of cellular energy
301 metabolism in response to perinatal injury.

302

303 Insult-specific transcriptomic patterns were also observed. Hx alone showed a positive
304 correlation exclusively with M1, which was negatively correlated in controls and broadly
305 distributed across the cerebellar cortex **(Fig. 3b, c)**. M1 was enriched for pathways related to
306 synaptic signaling and regulation, suggesting that Hx alters cerebellar circuit organization. In
307 contrast, MIA exposure alone (LPS-N) was positively associated with multiple M-patterns,
308 including M2, M4, and M9 **(Fig. 3b, c)**. Notably, pattern M4 was highly enriched in both LPS-N
309 and DH groups **(Fig. 3c)** and spatially localized to PCs and GCs **(Fig. 3b)**, consistent with
310 histological findings. M4 was linked to mitochondrial respiration and ATP production pathways,
311 indicating immune activation-induced metabolic stress **(Fig. 3d-e and Supplemental files)**. In
312 the DH group, however, none of the M-patterns showed significant correlation **(Fig. 3c)**, in
313 contrast to the distinct patterns observed with Hx or MIA alone. This loss of expected spatial
314 associations suggests that MIA modulates the cerebellar transcriptional response to Hx in a non-
315 additive manner – reorganizing rather than summing the molecular effects of each insult.

316

317 Collectively, these findings indicate that while Hx alone primarily disrupts synaptic signaling
318 pathways, prior MIA exposure reprograms cerebellar developmental trajectories in the context of
319 Hx, shifting the dominant molecular pathology toward the profound impairments in
320 mitochondrial respiration and cellular energy metabolism.

321

322 *Neonatal Hx Exacerbates Mitochondrial Dysfunction Primed by MIA*

323 Based on the observed mitochondrial-related transcriptional changes following MIA and
324 subsequent hypoxia, we hypothesized that MIA primes cerebellar mitochondrial function during
325 fetal development, increasing the tissue's susceptibility to hypoxic injury later in life. To test this,
326 we conducted Seahorse-based bioenergetic profiling of whole cerebellar tissue at P11 and P45,
327 capturing both the immediate metabolic response to oxygen deprivation and the long-term
328 consequences of recovery **(Fig. 4a)**. At P11, mitochondrial function did not differ significantly
329 across groups, However, by P45, DH mice exhibited a marked increase in proton leak relative to
330 both control and Sal-Hx mice, indicating persistent mitochondrial dysfunction and impaired
331 energy production as a result of the dual insult **(Fig. 4b-c)**.

332

333 Consistent with the bioenergetic findings, quantitative electron microscopy (EM) assessment
334 revealed distinct mitochondrial alterations across cerebellar cell types - GCs and PCs - in
335 response to single and serial insults at both neonatal and adulthood timepoints **(Fig. 4d)**. At P11,
336 GCs in both the DH and Sal-Hx groups exhibited reduced mitochondrial surface area, which
337 normalized by adulthood, indicating an acute but transient effect of Hx on GC mitochondria
338 **(Fig. 4g-h)**. In contrast, by P45, DH mice showed a sustained reduction in mitochondrial density

339 in both GCs and PCs, along with decreased mitochondrial surface area specifically in PCs. These
340 findings suggest a prolonged and cell type–specific mitochondrial impairment in DH mice, likely
341 driven by MIA pre-exposure **(Fig. 4e-f, i-l).**
342
343 We next conducted a qualitative EM assessment of mitochondria integrity in GCs and PCs at P11
344 and P45, using a severity scoring system ranging from 1 (healthy, dark blue) to 5 (severely
345 damaged/mitophagy, red)[37] **(Fig. 4m)**. In GCs, we observed progressive structural mitochondrial
346 damage across both single-hit and DH groups by adulthood, with the most pronounced injury in
347 groups exposed to Hx (Sal-Hx and DH) **(Fig. 4n)**. In contrast, PC mitochondrial damage observed
348 at P11 in single-hit groups (Sal-Hx and LPS-N) largely resolved by P45, indicating recovery over
349 time. However, in DH mice, PC mitochondria showed worsening injury, with a higher proportion
350 of severely damaged mitochondria persisting into adulthood **(Fig. 4o)**. These findings confirm
351 that hypoxia drives early mitochondrial injury in GCs, while MIA modulates and amplifies the
352 long-term mitochondrial response to hypoxia in both cerebellar cell types—ultimately leading to
353 cumulative and progressive damage, particularly in the DH group.
354
355 *MIA Reprograms Hypoxia-Induced S- to G2-Phase Shift in Neuronal Cell Cycle Dynamics*
356 Building on our findings of sustained mitochondrial damage, we next investigated the
357 downstream consequences for neuronal development. Mitochondrial dysfunction is known to
358 trigger cell cycle arrest through 'mitochondrial checkpoints' that regulate neuronal proliferation
359 and maturation [38]. Based on this, we hypothesized that the cerebellar developmental arrest
360 observed in the DH mouse arises from cell cycle abnormalities driven by impaired neuronal
361 energy production following combined exposure to MIA and hypoxia[38].

362

363 Distinct neuronal populations in the cerebellum have specialized metabolic demands and occupy
364 defined spatial niches. To capture the impact of metabolic stress on cell cycle regulation within
365 this context, we performed spatially resolved cell cycle analysis using Visium-based Tricycle,
366 enabling phase-specific mapping across intact tissue sections **(Fig. 5a)**. This approach revealed
367 layer-specific patterns of cell cycle dysregulation, highlighting how mitochondrial dysfunction
368 disrupts the spatial coordination of cerebellar development.

369

370 At P45, Hx alone led to an increased proportion of GCs arrested in the S-phase, with minimal
371 progression into the G2/M and M/G1 phases - indicating a disruption in normal cell cycle
372 progression **(Fig. 5b)**. In contrast, the DH condition resulted in GC accumulation in the G2
373 phase, suggestive of a blockade prior to mitotic entry **(Fig. 5b)** Notably, PCs appeared resistant
374 to these cell cycle disruptions, at least in terms of detectable phase-specific alterations. These
375 findings underscore that cerebellar developmental injury is not uniformly distributed, but instead
376 selectively impacts specific neuronal populations based on their vulnerability to metabolic and
377 environmental stressors.

378

379 To investigate the mechanisms driving these adult-phase cell cycle abnormalities, we conducted
380 targeted validation experiments at P11 - a developmental stage characterized by active GC
381 proliferation. These analyses revealed significantly elevated expression of the cyclin-dependent
382 kinase inhibitors p21 and p27 in the DH cerebellum **(Fig. 5c-d)**, consistent with early activation
383 of cell cycle arrest pathways and impaired progression through the late phases of the cell cycle.

384

385 Together, these findings indicate that MIA followed by Hx induces an early and persistent shift
386 toward cell cycle arrest during cerebellar development, with effects extending into adulthood.
387 This sustained disruption of normal cell cycle dynamics is consistent with the long-term
388 mitochondrial dysfunction and histological evidence of impaired neuronal maturation observed
389 in the DH cerebellum.
390
391 *Disrupted Cell–Cell Signaling Underlies Insult-Specific Rewiring of the Cerebellar Connectome*
392 Given that perinatal insults disrupt not only individual neuronal populations but also their
393 integration into broader cerebellar circuits, we next investigated how arrested neuronal
394 development affects circuit connectivity. The integrity of cerebellar function depends on precise
395 intercellular communication - particularly between GCs and PCs. We hypothesized that
396 disruptions in cell–cell signaling would both reflect and contribute to the circuit-level
397 dysfunction underlying the motor deficits observed in the DH model. To identify transcriptional
398 changes in intercellular communication, we applied LIANA (LIgand receptor ANalysis
399 frAmework) to the Visium transcriptomic dataset, enabling inference of ligand–receptor
400 interactions across cerebellar cell types **(Fig. 6a-d)**.
401
402 The Hx-only group exhibited a broad reduction in intercellular signaling, most prominently from
403 GCs to PCs **(Fig. 6a, b)**. These pathways were primarily associated with synaptic plasticity and
404 glutamatergic transmission. Notably, signaling involving GRM1 – a critical synaptic receptor
405 whose impairment is implicated in ASD-like phenotypes[39] – was diminished. Based on the
406 transcriptomic findings on reduced excitatory input, we performed synaptic architecture analysis

407 which revealed a marked reduction vGLUT2-positive (vGLUT2+) synaptic puncta within the
408 molecular layer of Sal-Hx mice compared to controls (**Fig. 6e, f**).
409
410 In contrast, the LPS-N group exhibited a pronounced signaling imbalance, characterized by
411 enhanced GC-to-PC communication alongside reduced PC-to-GC signaling **(Fig. 6c)**. These
412 altered interactions affected multiple systems, including pathways involved in cell adhesion and
413 the regulation of excitatory/inhibitory balance. Consistent with a state of increased excitatory
414 drive, LPS-N mice showed a significant elevation in vGLUT2+ density compared to both control
415 and Sal-Hx groups **(Fig. 6e, f)**. DH exposure produced an entirely distinct pattern of network
416 disruption, impacting pathways critical for progenitor proliferation and synaptic maturation. GC-
417 to-PC signaling was reduced relative to the LPS-N group, while PC-PC communication was
418 markedly increased **(Fig. 6d)**. Among the most significantly altered interactions was CALM1-
419 GRM4 glutamatergic signaling. Although overall vGLUT2+ levels in DH mice were comparable
420 to controls, their spatial distribution was abnormal – showing increased labeling along distal
421 dendrites - suggesting disrupted synaptic targeting and altered integration of excitatory input
422 **(Fig. 6e, f)**.
423
424 These findings show that perinatal insults disrupt cerebellar connectivity through distinct, insult-
425 specific alterations in intercellular signaling. Hx suppresses GC-to-PC communication and
426 reduces excitatory input; MIA enhances excitatory signaling in a dysregulated fashion; and DH
427 induces aberrant synaptic targeting alongside increased PC–PC connectivity, indicative of
428 maladaptive circuit remodeling. Collectively, these transcriptomic and structural alterations

429 implicate disrupted cell–cell communication as a core mechanism underlying circuit
430 dysmaturation and motor deficits in preterm brain injury.
431
432 *MIA Modifies the Neurobehavioral Impact of Neonatal Hx*
433 Given the disrupted GC–PC connectivity and motor learning deficits in DH mice, we asked
434 whether these microcircuit alterations extend to other cerebellar-dependent behaviors, focusing
435 on social interaction. Abnormal cerebellar connectivity is increasingly recognized as a hallmark
436 of neurodevelopmental disorders - including ASD - underscoring the cerebellum's influence on
437 social behavior [40]. We therefore assessed sociability with three-chamber social paradigm[41] (**Fig.**
438 **7a**). Continuous video recordings were analyzed in DeepLabCut™ for precise, automated
439 tracking of behavior in a modified 3-chamber apparatus (**Fig. 7b**). To further refine the assay, we
440 generated video-based heat maps that visualize chamber occupancy and movement
441 trajectories[41,42] (**Extended Data Fig. 3a-b**).
442
443 Sal-Hx mice exhibited a lack of sociability, showing a slight preference for the novel object over
444 the stranger mouse and spending the majority of their time in non-social areas (**Fig. 7c**). This
445 behavioral pattern is consistent with social withdrawal and an increased object-directed
446 exploratory drive. Similarly, LPS-N mice showed reduced sociability, with a more evenly
447 distributed pattern of exploration and comparable time spent across all three chambers **(Fig. 7c**
448 **and Extended Data Fig. 3b)**. Interestingly, DH mice demonstrated normal sociability, spending
449 significantly more time with the novel mouse than with the object - similar to controls. However,
450 their social behavior was qualitatively distinct: DH mice frequently reared on their hind limbs

451 while in proximity to the novel mouse, suggesting altered patterns of social engagement **(Fig. 7c**
452 **and Extended Data Fig. 3c)**.
453
454 We next examined cerebellar-associated motor impairments influenced general and spontaneous
455 exploratory behavior. To do this, we analyzed video recordings from the 10-minute-period
456 preceding the social test, during which mice explored the chambers freely in the absence of any
457 social or object stimuli. To capture overall exploratory drive, we computed a composite ratio that
458 compares time spent in open field areas to time spent stationary in the chamber corners or at gate
459 entrances. Lower ratio values reflected reduced exploratory behavior and a preference for
460 stationary or sheltered locations (**Fig. 7d-e**). Both Sal-Hx and DH mice exhibited significantly
461 lower exploration ratios compared to controls, with DH mice showing the most pronounced
462 deficits. These results suggest that early cerebellar-driven locomotor impairments may limit
463 spontaneous exploration, potentially contributing to altered social behavior and highlighting a
464 mechanistic link between motor dysfunction and impaired social engagement (**Fig. 7e**).
465
466 Overall, these findings highlight the distinct effects of individual early-life insults on sociability.
467 MIA exposure led to reduced social interaction, while neonatal hypoxia resulted in a lack of
468 sociability in the 3-chamber social approach test – both behavioral profiles consistent with ASD-
469 like features. Notably, while the combined immune and hypoxic challenge (DH) did not
470 significantly impair overall sociability, it resulted in qualitatively altered patterns of social
471 interaction and reduced exploratory behavior. The co-occurrence of motor and social/exploratory
472 deficits in the Sal-Hx and DH groups underscores the cerebellum's heightened vulnerability to
473 early-life insults and its central role in shaping complex neurodevelopmental phenotypes.

MIA Pre-Exposure Shifts Hx-Induced Motor Stereotypies toward Heightened Social Behavior

The pronounced social deficits observed in Sal-Hx mice, coupled with motor impairments and reduced exploratory behavior, suggest that motor dysfunction may influence the quality of social interactions. To further investigate the cerebellum's integrative role in motor and social domains, we analyzed specific kinematic features – defined as distinct patterns of motor movement – during the three-chamber social test.

To comprehensively characterize locomotor dynamics during the social exploration assay, we applied B-SOiD - an unsupervised, pose-based behavioral segmentation algorithm that identifies discrete kinematic motifs independent of spatial context **(Fig. 8a–b).** Using positional data from the snout, ears, and body center, B-SOiD classified behavior into 14 reproducible kinematic motifs (Clusters), each representing a recurring pattern of movement rather than a location-bound activity **(Fig. 8c, Table 4, Extended Data Fig. 4-1)**. A key strength of this approach is its ability to detect and classify motifs regardless of their location in the arena, enabling unbiased analysis of motif frequency and duration across different zones (e.g., social, object, or neutral). The 14 identified motifs captured a broad spectrum of behaviors, including high-velocity exploration (Clusters 2, 11, 12), perimeter scanning (Cluster 4), stationary investigation (Clusters 3, 7, 8, 10, 13), transitional movements (Clusters 1, 6, 9), and pauses or disengagement (Clusters 0, 5) **(Fig. 8c, Table 4, Extended Data Fig. 4-1).** This data-driven framework enables objective classification of motor strategies, including subtle movement patterns that may not be readily discernible through visual observation alone.

497 We hypothesized that the distinct social phenotypes observed following early-life insults would
498 correspond to unique kinematic profiles, reflecting cerebellar contributions to social behavior.
499 Our results support this hypothesis: mice exposed to Hx-only or DH exhibited distinct movement
500 signatures compared to controls **(Fig. 8d)**. Sal-Hx mice demonstrated an increased frequency of
501 stereotyped motor motifs (Clusters 1, 12, and 13), characterized by repetitive head and body
502 turning. These low-variability patterns were observed across all chambers, suggesting restricted
503 and inflexible exploration consistent with an ASD-like behaviors. In contrast, DH mice engaged
504 more frequently in dynamic, socially relevant motifs (Clusters 8, 7, and 2), including standing
505 and approach behaviors. These interaction-related actions occurred most prominently within the
506 social chamber, indicating a distinct and highly interactive social profile **(Fig. 8e, Extended**
507 **Data Fig. 4-2)**.
508
509 These findings demonstrate that early-life cerebellar insults fundamentally alter the organization
510 of movement during social behavior. The nature and timing of the insult dictate the extent and
511 pattern of neural circuit disruption, giving rise to distinct and measurable social behavioral
512 phenotypes.
513
514 **Discussion**
515 This study establishes a mechanistic framework linking both the isolated and sequential
516 occurrence of MIA and Hx to distinct patterns of disrupted cerebellar development and
517 behavioral outcomes. By delineating how these insults converge on the developmental trajectory
518 of neuronal progenitors, we present a translationally relevant model that illuminates context-

specific vulnerabilities of the developing cerebellum and identifies pathways associated with abnormal neurobehavior, as well as critical windows for intervention.

Preterm birth remains a leading cause of neurodevelopmental disability worldwide[43]. Although advances in neonatal care have reduced the incidence of overt structural brain injury, more subtle yet persistent forms of developmental dysregulation – particularly within cerebellar circuits essential for motor, cognitive, and affective function[34] – have emerged. The heterogeneous etiologies of preterm birth give rise to diverse patterns of brain vulnerability, emphasizing the need to move beyond one-size-fits-all models of encephalopathy.

The significance of this study lies in the use of the DH mouse model that mirrors key cellular and molecular alterations observed in the human preterm cerebellum. Through parallel analyses in both species, we validated the model's relevance by identifying convergent cellular and molecular signatures of injury. Conserved DEGs revealed enrichment in pathways central to circuit assembly and cerebellar function. This molecular alignment underscores the model's utility for probing gene regulatory networks implicated in preterm brain injury and highlights potential biomarkers and therapeutic targets.

Moreover, the identification of insult-specific molecular and cellular alterations reinforces the importance of stratifying preterm infants based on underlying etiological factors – such as perinatal inflammation or hypoxia – to refine risk assessment and inform precision interventions.

541 A key insight from this work is that both the timing and sequence of perinatal insults critically
542 shape the trajectory of cerebellar development. Sequential exposure to MIA followed by
543 postnatal Hx - common in preterm deliveries - produces a neurodevelopmental signature that is
544 mechanistically and functionally distinct from that of isolated insults. This shift in focus from the
545 identity of insults to their chronology has broad implications for experimental modeling and
546 clinical risk stratification
547
548 Our findings also highlight the cerebellum's dual vulnerability to disruptions in afferent and
549 efferent signaling. Injury from isolated hypoxia led to increased locomotor missteps, consistent
550 with disruptions in proprioceptive and sensorimotor input via mossy fibers from the
551 spinocerebellar tract[44]. In contrast, adaptive motor behavior – dependent on cerebellar output to
552 the red nucleus and thalamocortical circuits[45,46] – was selectively impaired in DH mice,
553 suggesting a breakdown in long-range connectivity and integrative cerebellar function. This
554 dissociation, wherein Hx impairs coordination while DH affects motor learning, illustrates
555 circuit-specific vulnerabilities shaped by the timing of injury. Recognizing these distinctions may
556 improve neurodevelopmental phenotyping in preterm infants and guide the development of
557 targeted interventions.
558
559 We further show that MIA and Hx exert temporally and mechanistically distinct effects on
560 cerebellar maturation. Hypoxia primarily disrupted differentiated GCs, while MIA altered PC
561 morphology and delayed GCP maturation. The DH condition exacerbated both injury profiles,
562 indicating a synergistic – not merely additive - effect. This compounded vulnerability likely
563 underlies the more severe structural and motor deficits observed in DH-exposed offspring,

aligning with clinical observations of heightened ataxia and sensorimotor dysfunction in preterm infants[47,48,20].

A particularly intriguing and unexpected finding is the preservation of sociability in DH mice despite marked cerebellar dysfunction and impaired motor learning. In contrast, mice exposed solely to Hx exhibited significant social deficits, consistent with prior models of hypoxia-induced ASD-like behavior[49]. One possible explanation is that prenatal MIA shifts the developmental timing of vulnerable neuronal populations, altering their susceptibility to subsequent hypoxic injury. Rather than compounding the effects of Hx, MIA may reshape cellular sensitivity, thus mitigating social impairments. These findings underscore the importance of injury timing and developmental context in modeling complex neurodevelopmental disorders.

A critical implication of this work is the need to disentangle motor impairments from primary deficits in social cognition when interpreting atypical social behaviors. This distinction is especially relevant for conditions like cerebral palsy, where motor dysfunction frequently co-occurs with social developmental delays[50,51]. Social interaction depends on the precise coordination of gaze, facial expression, gesture, and posture- behaviors requiring intact sensorimotor integration[34,52]. Disruption in cerebellar or corticospinal circuits may lead to social abnormalities that are misattributed to deficits in social cognition. Mechanistically informed behavioral phenotyping is essential to distinguish between motor-driven and centrally mediated social dysfunction, refine diagnostic criteria, and reduce the risk of diagnostic overshadowing. This distinction also has therapeutic implications, guiding interventions that target both motor and social domains.

587

588 Importantly, insult-specific kinematic features identified in this study may serve as early
589 biomarkers of cerebellar dysfunction, enabling timely detection of atypical neurodevelopment in
590 high-risk populations. These findings emphasize the cerebellum's central role not only in motor
591 control but also as a regulator of developmental timing and adaptive plasticity. Specific
592 behavioral and movement patterns correlate with cerebellar output to regions such as the
593 thalamus, ventral tegmental area, and medial prefrontal cortex, offering valuable indicators of
594 broader network health[53,54]. For instance, neonatal Hx impairs glutamatergic signaling
595 (vGLUT2+), leading to behavioral profiles marked by motor rigidity and social withdrawal,
596 consistent with ASD-like traits[,54]. In contrast, prior MIA redirects hypoxic injury to PCs and
597 their mitochondria, disrupting GABAergic output and excitatory-inhibitory balance[55] –
598 mechanisms likely underlying the motor learning deficits observed in DH mice.

599

600 This study underscores the cerebellum's vulnerability to sequential developmental insults and
601 establishes the DH model as a valuable platform for mechanistic and therapeutic research. By
602 linking molecular disruptions to distinct behavioral phenotypes, we offer a translationally
603 relevant framework for studying neurodevelopmental disorders in the context of prematurity and
604 early-life stress. Targeting mitochondrial dysfunction or synaptic disorganization during critical
605 windows may enable early intervention. Importantly, the co-occurrence of motor and social
606 deficits further highlights the need for integrated, multi-domain therapeutic strategies.
607 Collectively, these findings challenge traditional paradigms that rely on structural imaging or
608 static lesion identification to define preterm brain injury. Instead, they advocate for mechanistic
609 phenotyping based on developmental timing, functional circuit engagement, and longitudinal

outcomes. Framing preterm encephalopathy through this lens may enable targeted individualized prognostication and enable more effective, developmentally timed interventions during critical windows of cerebellar plasticity. Future studies should assess whether timely intervention can restore cerebellar development and function.

Resource availability

Lead contact

Further information and requests for resources and reagents should be directed to and will be fulfilled by the lead contact, Panagiotis Kratimenos, M.D., Ph.D. (pankratimenos@gwu.org, Panagiotis.Kratimenos@childrensnational.org)

Materials availability

This study did not generate new unique reagents.

Data and code availability

Bulk and spatial RNA-seq data analysis from cerebellar mouse and human tissue have been deposited in the NoCodeSeg repository and are publicly available. The accession number is listed in the methods.

Any additional information required to reanalyze the data reported in this paper is available from the lead contact upon request.

Acknowledgments

This work was supported by the Raynor Cerebellum Project (P.K.), R37NS109478 (Javits Award; V.G.), K12HD001399 Child Health Research Career Development Award (CHRCDA, P.K.), American SIDS Institute (P.K.), a Children's National Board of Visitors' Grant (P.K.) and 1R21NS135088 (I.K.). This study was also supported by the District of Columbia Intellectual and Developmental Disabilities Research Center (DC-IDDRC) award P50HD105328; (V.G.) from the Eunice Kennedy Shriver National Institute of Child Health and Human Development. We thank the Neurobehavioral Evaluation Core of the Intellectual and Developmental Disabilities Research Center at Children's National Hospital for training and supervision for behavioral testing and Dr. Jacqueline Crawley of the University of California Davis MIND Institute for her assistance with manuscript preparation.

Declaration of interests

The authors declare no competing interests.

Author contributions

P.K., conceived and designed the study. G.San., G.Sim., P.K., I.K., J.G., and K.W. performed the experiments and collected the data. K.W., G.Stein., R.V., D.S., H.S., E.G. and A.S. conducted the data analysis. G.San., G.Sim., P.K., N.W., M.T., C.B., and I.K. contributed to the interpretation of the results and provided critical feedback. G.San., G.Sim., V.G. and P.K. drafted the manuscript, and all authors contributed to the revisions and approved the final version.

690 **References**

691 1 Pascoe, L., Burnett, A. C. & Anderson, P. J. Cognitive and academic outcomes of children born
692 extremely preterm. *Semin Perinatol* **45**, 151480 (2021).
693 https://doi.org/10.1016/j.semperi.2021.151480
694 2 Inder, T. E., Volpe, J. J. & Anderson, P. J. Defining the Neurologic Consequences of Preterm
695 Birth. *N Engl J Med* **389**, 441-453 (2023). https://doi.org/10.1056/NEJMra2303347
696 3 Cheong, J. L. Y. *et al.* Temporal Trends in Neurodevelopmental Outcomes to 2 Years After
697 Extremely Preterm Birth. *JAMA Pediatrics* **175** (2021/10/01).
698 https://doi.org/10.1001/jamapediatrics.2021.2052
699 4 Romero, R. *et al.* Prevalence and clinical significance of sterile intra-amniotic inflammation in
700 patients with preterm labor and intact membranes. *Am J Reprod Immunol* **72**, 458-474 (2014).
701 https://doi.org/10.1111/aji.12296
702 5 Agrawal, V. & Hirsch, E. Intrauterine infection and preterm labor. *Semin Fetal Neonatal Med* **17**,
703 12-19 (2012). https://doi.org/10.1016/j.siny.2011.09.001
704 6 Erlebacher, A. Immunology of the maternal-fetal interface. *Annu Rev Immunol* **31**, 387-411
705 (2013). https://doi.org/10.1146/annurev-immunol-032712-100003
706 7 Lu-Culligan, A. & Iwasaki, A. The Role of Immune Factors in Shaping Fetal Neurodevelopment.
707 *Annu Rev Cell Dev Biol* **36**, 441-468 (2020). https://doi.org/10.1146/annurev-cellbio-021120-
708 033518
709 8 Kratimenos, P., Sanidas, G., Simonti, G., Byrd, C. & Gallo, V. The shifting landscape of the
710 preterm brain. *Neuron* **113** (2025/07/09). https://doi.org/10.1016/j.neuron.2025.03.024
711 9 Zuckerman, L. & Weiner, I. Maternal immune activation leads to behavioral and pharmacological
712 changes in the adult offspring. *J Psychiatr Res* **39**, 311-323 (2005).
713 https://doi.org/10.1016/j.jpsychires.2004.08.008
714 10 Bitanihirwe, B. K., Peleg-Raibstein, D., Mouttet, F., Feldon, J. & Meyer, U. Late prenatal
715 immune activation in mice leads to behavioral and neurochemical abnormalities relevant to the
716 negative symptoms of schizophrenia. *Neuropsychopharmacology* **35**, 2462-2478 (2010).
717 https://doi.org/10.1038/npp.2010.129
718 11 Pendyala, G. *et al.* Maternal Immune Activation Causes Behavioral Impairments and Altered
719 Cerebellar Cytokine and Synaptic Protein Expression. *Neuropsychopharmacology* **42**, 1435-1446
720 (2017). https://doi.org/10.1038/npp.2017.7
721 12 Lacaille, H. *et al.* Impaired Interneuron Development in a Novel Model of Neonatal Brain Injury.
722 *eNeuro* **6** (2019). https://doi.org/10.1523/ENEURO.0300-18.2019
723 13 Sathyanesan, A., Kundu, S., Abbah, J. & Gallo, V. Neonatal brain injury causes cerebellar
724 learning deficits and Purkinje cell dysfunction. *Nat Commun* **9**, 3235 (2018).
725 https://doi.org/10.1038/s41467-018-05656-w
726 14 MK, M., M, A., JE, L. & CR, N. Long-term neurodevelopmental outcomes after intrauterine and
727 neonatal insults: a systematic review - PubMed. *Lancet (London, England)* **379** (02/04/2012).
728 https://doi.org/10.1016/S0140-6736(11)61577-8
729 15 Volpe, J. J. Cerebellum of the premature infant: rapidly developing, vulnerable, clinically
730 important. *J Child Neurol* **24**, 1085-1104 (2009). https://doi.org/10.1177/0883073809338067
731 16 Sokolov, A. A., Miall, R. C. & Ivry, R. B. The Cerebellum: Adaptive Prediction for Movement
732 and Cognition. *Trends Cogn Sci* **21**, 313-332 (2017). https://doi.org/10.1016/j.tics.2017.02.005
733 17 Popa, L. S. & Ebner, T. J. Cerebellum, Predictions and Errors. *Front Cell Neurosci* **12**, 524
734 (2018). https://doi.org/10.3389/fncel.2018.00524
735 18 Wang, L. A. L., Petrulla, V., Zampella, C. J., Waller, R. & Schultz, R. T. Gross motor impairment
736 and its relation to social skills in autism spectrum disorder: A systematic review and two meta-
737 analyses. *Psychol Bull* **148**, 273-300 (2022). https://doi.org/10.1037/bul0000358

19 Craig, F. *et al.* Characterization of Autism Spectrum Disorder (ASD) subtypes based on the relationship between motor skills and social communication abilities. *Hum Mov Sci* **77**, 102802 (2021). https://doi.org/10.1016/j.humov.2021.102802

20 Albayrak, B. *et al.* Ataxia Rating Scales Reveal Increased Scores in Very Preterm Born 5-6-Year-Old Preschool Children and Young Adults. *Cerebellum* **22**, 877-887 (2023). https://doi.org/10.1007/s12311-022-01463-8

21 O'Halloran, C. J., Kinsella, G. J. & Storey, E. The cerebellum and neuropsychological functioning: a critical review. *J Clin Exp Neuropsychol* **34**, 35-56 (2012). https://doi.org/10.1080/13803395.2011.614599

22 Schmahmann, J. D., Weilburg, J. B. & Sherman, J. C. The neuropsychiatry of the cerebellum - insights from the clinic. *Cerebellum* **6**, 254-267 (2007). https://doi.org/10.1080/14734220701490995

23 van der Heijden, M. E., Gill, J. S. & Sillitoe, R. V. Abnormal Cerebellar Development in Autism Spectrum Disorders. *Dev Neurosci* **43**, 181-190 (2021). https://doi.org/10.1159/000515189

24 Otis, E. M. & Brent, R. Equivalent ages in mouse and human embryos. *Anat Rec* **120**, 33-63 (1954). https://doi.org/10.1002/ar.1091200104

25 Chen, V. S. *et al.* Histology Atlas of the Developing Prenatal and Postnatal Mouse Central Nervous System, with Emphasis on Prenatal Days E7.5 to E18.5. *Toxicol Pathol* **45**, 705-744 (2017). https://doi.org/10.1177/0192623317728134

26 Theiler, K. The house mouse: atlas of embryonic development. *Springer-Verlag* (1989).

27 Rice, D. & Barone, S., Jr. Critical periods of vulnerability for the developing nervous system: evidence from humans and animal models. *Environ Health Perspect* **108 Suppl 3**, 511-533 (2000). https://doi.org/10.1289/ehp.00108s3511

28 True, H., Blanton, M., Sureshchandra, S. & Messaoudi, I. Monocytes and macrophages in pregnancy: The good, the bad, and the ugly. *Immunol Rev* **308**, 77-92 (2022). https://doi.org/10.1111/imr.13080

29 Jablonska, B. *et al.* Sirt2 promotes white matter oligodendrogenesis during development and in models of neonatal hypoxia. *Nat Commun* **13**, 4771 (2022). https://doi.org/10.1038/s41467-022-32462-2

30 Forbes, T. A. *et al.* Environmental enrichment ameliorates perinatal brain injury and promotes functional white matter recovery. *Nat Commun* **11**, 964 (2020). https://doi.org/10.1038/s41467-020-14762-7

31 Kundu, S. *et al.* Cerebellar Purkinje Cell Activity Regulates White Matter Response and Locomotor Function after Neonatal Hypoxia. *J Neurosci* **45** (2025). https://doi.org/10.1523/JNEUROSCI.0899-24.2024

32 Mishra, I. *et al.* The cerebellum modulates thirst. *Nat Neurosci* **27**, 1745-1757 (2024). https://doi.org/10.1038/s41593-024-01700-9

33 Sathyanesan, A., Kratimenos, P. & Gallo, V. Disruption of neonatal Purkinje cell function underlies injury-related learning deficits. *Proc Natl Acad Sci U S A* **118** (2021). https://doi.org/10.1073/pnas.2017876118

34 Sathyanesan, A. *et al.* Emerging connections between cerebellar development, behaviour and complex brain disorders. *Nat Rev Neurosci* **20**, 298-313 (2019). https://doi.org/10.1038/s41583-019-0152-2

35 Sathyanesan, A. & Gallo, V. Cerebellar contribution to locomotor behavior: A neurodevelopmental perspective. *Neurobiology of learning and memory* **165** (2018 Apr 30). https://doi.org/10.1016/j.nlm.2018.04.016

36 Jia, E. *et al.* Effects of brain tissue section processing and storage time on gene expression. *Anal Chim Acta* **1142**, 38-47 (2021). https://doi.org/10.1016/j.aca.2020.10.046

37 Coughlin, L., Morrison, R. S., Horner, P. J. & Inman, D. M. Mitochondrial morphology differences and mitophagy deficit in murine glaucomatous optic nerve. *Invest Ophthalmol Vis Sci* **56**, 1437-1446 (2015). https://doi.org/10.1167/iovs.14-16126

38 Antico Arciuch, V. G., Elguero, M. E., Poderoso, J. J. & Carreras, M. C. Mitochondrial regulation of cell cycle and proliferation. *Antioxid Redox Signal* **16**, 1150-1180 (2012). https://doi.org/10.1089/ars.2011.4085

39 Nisar, S. *et al.* Genetics of glutamate and its receptors in autism spectrum disorder. *Mol Psychiatry* **27**, 2380-2392 (2022). https://doi.org/10.1038/s41380-022-01506-w

40 Hanaie, R. *et al.* Aberrant Cerebellar-Cerebral Functional Connectivity in Children and Adolescents With Autism Spectrum Disorder. *Front Hum Neurosci* **12**, 454 (2018). https://doi.org/10.3389/fnhum.2018.00454

41 Yang, M., Silverman, J. L. & Crawley, J. N. Automated three-chambered social approach task for mice. *Curr Protoc Neurosci* **Chapter 8**, Unit 8 26 (2011). https://doi.org/10.1002/0471142301.ns0826s56

42 Lauer, J. *et al.* Multi-animal pose estimation, identification and tracking with DeepLabCut. *Nat Methods* **19**, 496-504 (2022). https://doi.org/10.1038/s41592-022-01443-0

43 Mitha, A. *et al.* Neurological development in children born moderately or late preterm: national cohort study. *BMJ* **384** (2024-01-24). https://doi.org/10.1136/bmj-2023-075630

44 Pop, I. V. *et al.* Structure of Long-Range Direct and Indirect Spinocerebellar Pathways as Well as Local Spinal Circuits Mediating Proprioception. *J Neurosci* **42**, 581-600 (2022). https://doi.org/10.1523/JNEUROSCI.2157-20.2021

45 Tanaka, Y. H. *et al.* Thalamocortical Axonal Activity in Motor Cortex Exhibits Layer-Specific Dynamics during Motor Learning. *Neuron* **100**, 244-258 e212 (2018). https://doi.org/10.1016/j.neuron.2018.08.016

46 Schafer, C. B., Gao, Z., De Zeeuw, C. I. & Hoebeek, F. E. Temporal dynamics of the cerebello-cortical convergence in ventro-lateral motor thalamus. *J Physiol* **599**, 2055-2073 (2021). https://doi.org/10.1113/JP280455

47 Niutanen, U., Harra, T., Lano, A. & Metsaranta, M. Systematic review of sensory processing in preterm children reveals abnormal sensory modulation, somatosensory processing and sensory-based motor processing. *Acta Paediatr* **109**, 45-55 (2020). https://doi.org/10.1111/apa.14953

48 Spittle, A. J. & Orton, J. Cerebral palsy and developmental coordination disorder in children born preterm. *Semin Fetal Neonatal Med* **19**, 84-89 (2014). https://doi.org/10.1016/j.siny.2013.11.005

49 Driscoll, D. J. O., Felice, V. D., Kenny, L. C., Boylan, G. B. & O'Keeffe, G. W. Mild prenatal hypoxia-ischemia leads to social deficits and central and peripheral inflammation in exposed offspring. *Brain Behav Immun* **69**, 418-427 (2018). https://doi.org/10.1016/j.bbi.2018.01.001

50 Whittingham, K., Fahey, M., Rawicki, B. & Boyd, R. The relationship between motor abilities and early social development in a preschool cohort of children with cerebral palsy. *Res Dev Disabil* **31**, 1346-1351 (2010). https://doi.org/10.1016/j.ridd.2010.07.006

51 Voorman, J. M., Dallmeijer, A. J., Van Eck, M., Schuengel, C. & Becher, J. G. Social functioning and communication in children with cerebral palsy: association with disease characteristics and personal and environmental factors. *Dev Med Child Neurol* **52**, 441-447 (2010). https://doi.org/10.1111/j.1469-8749.2009.03399.x

52 Stoodley, C. J. & Tsai, P. T. Adaptive Prediction for Social Contexts: The Cerebellar Contribution to Typical and Atypical Social Behaviors. *Annu Rev Neurosci* **44**, 475-493 (2021). https://doi.org/10.1146/annurev-neuro-100120-092143

53 Odorcyk, F. K. *et al.* Differential Age-Dependent Mitochondrial Dysfunction, Oxidative Stress, and Apoptosis Induced by Neonatal Hypoxia-Ischemia in the Immature Rat Brain. *Mol Neurobiol* **58**, 2297-2308 (2021). https://doi.org/10.1007/s12035-020-02261-1

54 Van Overwalle, F. Social and emotional learning in the cerebellum. *Nat Rev Neurosci* **25**, 776-791 (2024). https://doi.org/10.1038/s41583-024-00871-5

55 Dacre, J. *et al.* A cerebellar-thalamocortical pathway drives behavioral context-dependent movement initiation. *Neuron* **109**, 2326-2338 e2328 (2021). https://doi.org/10.1016/j.neuron.2021.05.016

Figure 1

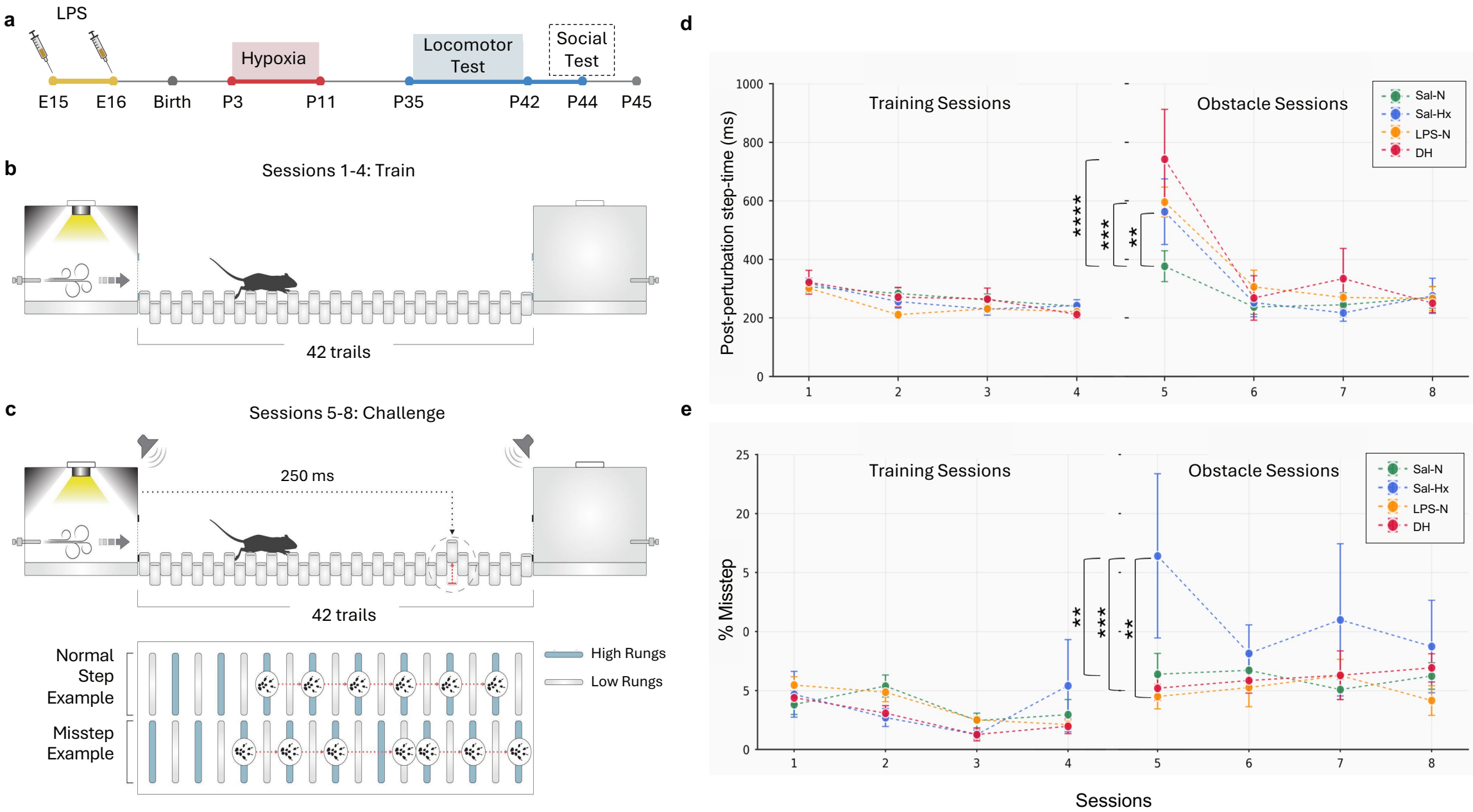
a
LPS
Hypoxia
Locomotor Test
Social Test
E15
E16
Birth
P3
P11
P35
P42
P44
P45
b
Sessions 1-4: Train
42 trails
c
Sessions 5-8: Challenge
250 ms
42 trails
Normal Step Example
Misstep Example
High Rungs
Low Rungs
d
Training Sessions
Obstacle Sessions
Post-perturbation step-time (ms)
Sal-N
Sal-Hx
LPS-N
DH
e
Training Sessions
Obstacle Sessions
% Misstep
Sessions

840 **Figure 1 - MIA Exacerbates Hypoxia-induced Long-term Cerebellar Locomotor Deficits: a,**
841 experimental paradigm of the double-hit (DH) mouse model. Dams are injected intraperitoneally
842 with lipopolysaccharide (LPS) or Saline at E15 and E16. Pups are exposed to prolonged hypoxia
843 (Hx) or normal oxygen (N) postnatally from P3 to P11. **b-c,** Schematic side view of the
844 ErasmusLadder paradigm used to test cerebellar-specific locomotor deficits in P45 mice. The
845 ErasmusLadder cerebellar motor learning assay consists of 8 sessions of 42 trials per session. The
846 mouse crosses the horizontal ladder, moving from the origin box to the goal box. Sessions 1-4 are
847 training sessions, with no perturbance present (**b**). Sessions 5-8 are challenge sessions in which a
848 sound cue, an obstacle consisting of a raised rung on the ladder, or both, are presented randomly
849 to the mouse during trials (**c**). Bottom image: schematic representation of normal step pattern (top)
850 and misstep pattern (bottom). The misstep parameter evaluates motor coordination. Circles with
851 paw indicate mouse limb positioning. **d,** Graph indicating absolute learning step-time (reaction to
852 the obstacle) by ErasmusLadder session assessed as a function of post-perturbation step-times (y-
853 axis) by session (x-axis). Groups performed similarly during the Training sessions. Step time
854 differed between groups during the obstacle sessions: Sal-N vs LPS: ***p = 0.0002; Sal-N vs Hx-
855 Sal: **p = 0.0038; Sal-N vs DH: ****p < .0001. **e**, Misstep percentage (y-axis) by session (x-axis)
856 assessed by ErasmusLadder for all four mouse groups. Sal-Hx vs. Sal-N: **p = 0.0019; Sal-Hx vs
857 LPS-N: ***p = 0.0008; Sal-Hx vs DH: **p = 0.0019; ns, non-significant. For **d** and **e**, n=10-15
858 animals per group; two-way repeated measures (RM) ANOVA with Tukey's multiple comparisons
859 test (additional statistics in Supplemental File). Data are represented as mean ± s.d. DH, double hit
860 LPS-Hx; E, embryonal; P, postnatal; Sal, saline; LPS, lipopolysaccharide; ms, milliseconds; N,
861 normoxia; Hx, hypoxia.

Figure 2

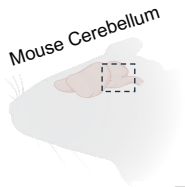
Mouse Cerebellum

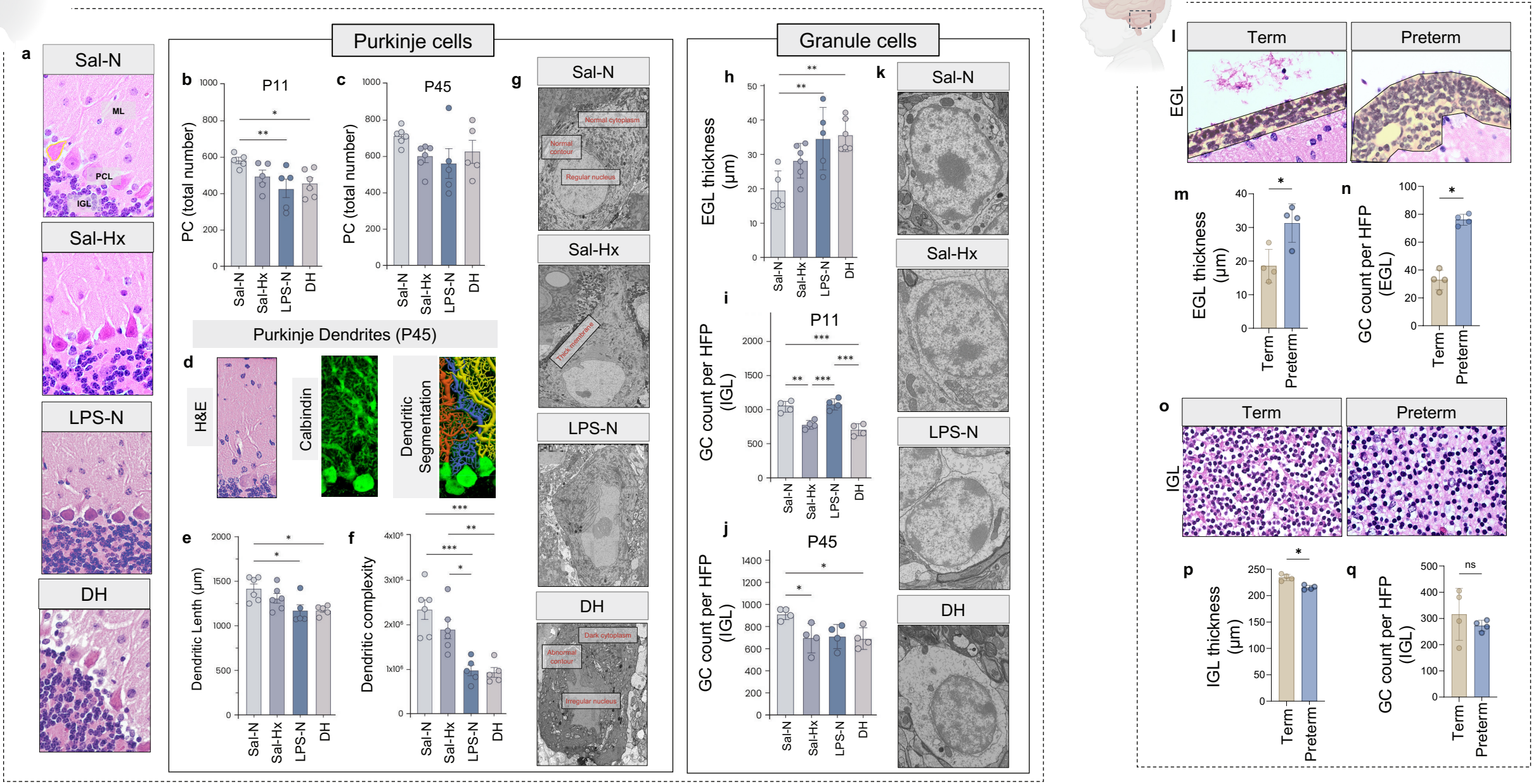
a
Sal-N
ML
PCL
IGL
Sal-Hx
LPS-N
DH
Purkinje cells
b
P11
PC (total number)
Sal-N
Sal-Hx
LPS-N
DH
c
P45
PC (total number)
Purkinje Dendrites (P45)
d
H&E
Calbindin
Dendritic Segmentation
e
Dendritic Lenth (µm)
f
Dendritic complexity
g
Normal cytoplasm
Normal contour
Regular nucleus
Thick membrane
Dark cytoplasm
Abnormal contour
Irregular nucleus
Granule cells
h
EGL thickness (µm)
i
P11
GC count per HFP (IGL)
j
P45
GC count per HFP (IGL)
k
Human Cerebellum
l
Term
Preterm
EGL
m
EGL thickness (µm)
n
GC count per HFP (EGL)
o
IGL
p
IGL thickness (µm)
q
GC count per HFP (IGL)
ns

862 **Figure 2 - Prematurity Insults Disrupt Cerebellar Cytoarchitecture and Mimic Human**
863 **Preterm Pathology: a**, Representative 40x magnification H&E images of neuropathological
864 qualitative analysis of Purkinje cells (PCs) and granule cells (GCs); yellow contour evidenced
865 PC soma, cerebellar layers are labelled; note: DH exhibits rarified neuropil and shrunken PC
866 somas. **b-c,** Mouse cerebellar histological analysis showing, PC total number at two timepoints –
867 P11 (**b**) and P45 (**c**). **d,** Schematic illustration of dendritic arborization quantification: on the left
868 panel, H&E-stained section; middle panel, Calbindin-stained representative PC imaged in
869 confocal microscope; right panel, user-guided dendritic tracing example using Neurolucida 360
870 (all images are 40x magnification). **e-f,** Graphs displaying dendritic length (**e**) and complexity (**f**)
871 at P45. **g,** Representative electron microscopy images from neuropathological qualitative
872 analysis of PC soma; note: thicker membrane in Sal-Hx mice and darker cytoplasm and disrupted
873 PC contour in DH mice. **h**, EGL thickness (only at P11, since the EGL disappears by P20). **i-j**,
874 IGL layer GCs number at P11 (**i**) and at P45 (**j**). **k**, Representative electron microscopy images
875 from neuropathological qualitative analysis of GC soma; note: DH group exhibits karyorrhexis
876 nuclei **l-n,** Human cerebellar histological analysis showing **l,** Representative 40X magnification
877 H&E images of EGL – marked in yellow. **m-n,** Graphs displaying the EGL thickness **(m)** and
878 EGL layer GCP number **(n)**. **o,** Representative 40X magnification H&E images of IGL. **p-q**
879 Graphs displaying the IGL thickness **(p)** and IGL layer GP number **(q)**. For **b-j**, n=4-5 per
880 mouse group. For **b-c**, one-way ANOVA with uncorrected Fisher's LSD. For **e, f,** and **h-j,** one-
881 way ANOVA with Tukey's multiple comparisons test (statistics in Supplemental File). For **m-q**,
882 n=4 term and n=4 preterm human subjects. For **m-n, p-q**, an unpaired t test was used. *$p < 0.05$,
883 **$p < 0.005$, ***$p < 0.0005$. Data are represented as mean ± s.d; EGL, external granule layer;
884 GC, granule cell; HPF, high power field at 40x magnification; H&E, hematoxylin-eosin; Hx,

885 hypoxia; IGL, internal granule layer; LPS, lipopolysaccharide; ML, molecular layer; N,
886 normoxia; P, postnatal; PC, Purkinje cell; PCL, Purkinje cell layer; Sal, saline; WM, white
887 matter.
888
889
890
891
892
893
894
895
896
897
898
899
900

Figure 3

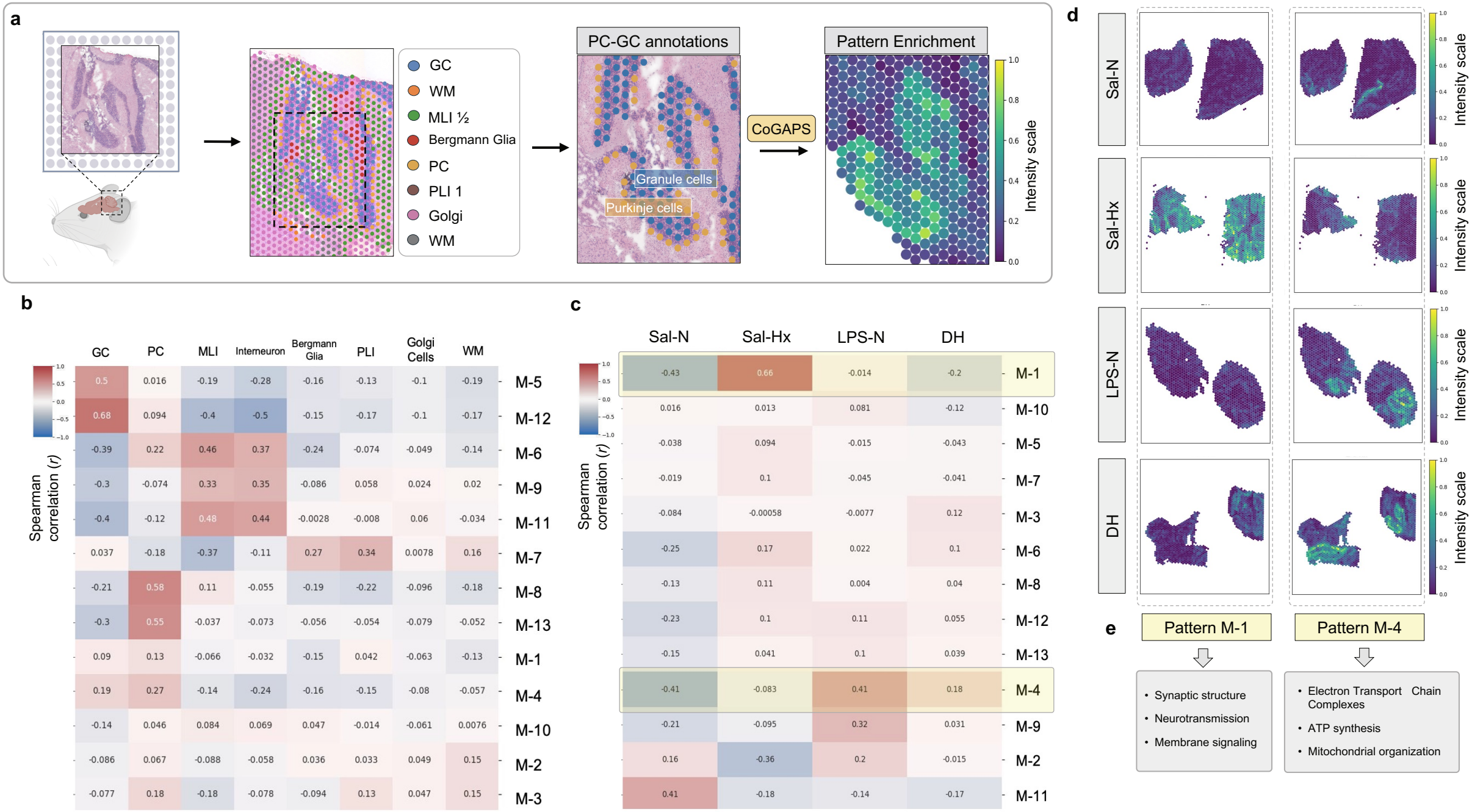

a
GC
WM
MLI ½
Bergmann Glia
PC
PLI 1
Golgi
WM
PC-GC annotations
Granule cells
Purkinje cells
CoGAPS
Pattern Enrichment
Intensity scale
b
Spearman correlation (r)
GC PC MLI Interneuron Bergmann Glia PLI Golgi Cells WM
M-5 0.5 0.016 -0.19 -0.28 -0.16 -0.13 -0.1 -0.19
M-12 0.68 0.094 -0.4 -0.5 -0.15 -0.17 -0.1 -0.17
M-6 -0.39 0.22 0.46 0.37 -0.24 -0.074 -0.049 -0.14
M-9 -0.3 -0.074 0.33 0.35 -0.086 0.058 0.024 0.02
M-11 -0.4 -0.12 0.48 0.44 -0.0028 -0.008 0.06 -0.034
M-7 0.037 -0.18 -0.37 -0.11 0.27 0.34 0.0078 0.16
M-8 -0.21 0.58 0.11 -0.055 -0.19 -0.22 -0.096 -0.18
M-13 -0.3 0.55 -0.037 -0.073 -0.056 -0.054 -0.079 -0.052
M-1 0.09 0.13 -0.066 -0.032 -0.15 0.042 -0.063 -0.13
M-4 0.19 0.27 -0.14 -0.24 -0.16 -0.15 -0.08 -0.057
M-10 -0.14 0.046 0.084 0.069 0.047 -0.014 -0.061 0.0076
M-2 -0.086 0.067 -0.088 -0.058 0.036 0.033 0.049 0.15
M-3 -0.077 0.18 -0.18 -0.078 -0.094 0.13 0.047 0.15
c
Spearman correlation (r)
Sal-N Sal-Hx LPS-N DH
M-1 -0.43 0.66 -0.014 -0.2
M-10 0.016 0.013 0.081 -0.12
M-5 -0.038 0.094 -0.015 -0.043
M-7 -0.019 0.1 -0.045 -0.041
M-3 -0.084 -0.00058 -0.0077 0.12
M-6 -0.25 0.17 0.022 0.1
M-8 -0.13 0.11 0.004 0.04
M-12 -0.23 0.1 0.11 0.055
M-13 -0.15 0.041 0.1 0.039
M-4 -0.41 -0.083 0.41 0.18
M-9 -0.21 -0.095 0.32 0.031
M-2 0.16 -0.36 0.2 -0.015
M-11 0.41 -0.18 -0.14 -0.17
d
Sal-N
Sal-Hx
LPS-N
DH
Intensity scale
e
Pattern M-1
Pattern M-4
• Synaptic structure
• Neurotransmission
• Membrane signaling
• Electron Transport Chain Complexes
• ATP synthesis
• Mitochondrial organization

901 **Figure 3 - Insult-Specific Alterations in Cerebellar Developmental Programs Revealed by**
902 **Spatial Transcriptomics: a**, Schematic illustration of pipeline for mouse-derived CoGAPS
903 pattern expression. Left image show H&E-stained mouse cerebellar tissue stemming from a
904 mouse brain illustration, followed by a representative example of annotated cerebellar tissue 10x
905 magnified. 40x magnified H&E-stained image of cerebellar tissue for granule cell annotation
906 (blue) and Purkinje cell annotations (orange). Right image, representative example of the same
907 tissue area after CoGAPS loading showing gene expression level in tissue. Expression levels
908 (intensity scale) ranging from low (blue) to high (yellow). **b**, Heatmaps displaying the Spearman
909 correlation (*r*) of the mouse CoGAPS patterns with the DH insults. **c,** Heatmaps displaying the
910 Spearman correlation (*r*) of the mouse CoGAPS patterns with specific cerebellar cell
911 populations. Highlighted in yellow are two patterns of interest (M-1 and M-4) for their insult-
912 specific correlation. **d**, Representative image of whole tissue expression patterns (Pattern M-1
913 and M-4) following Visium assay and CoGAPS loading in all experimental groups. Expression
914 levels (intensity scale) ranging from low (blue) to high (yellow). **e**, Schematic illustration
915 displaying the main Gene Ontology-identified biological functions associated with the genes in
916 the two highlighted patterns (Pattern M-1 and M-4). For **b** and **c**, Spearman correlation (*r*) scale
917 ranging from 1 (red, high positive correlation) to -1 (blue, high negative correlation). $n = 2$ per
918 group. CoGAPS, Coordinated Gene Activity in Pattern Sets; DH, double-hit; GC, Granule cell;
919 Hx, hypoxia; LPS, lipopolysaccharide; M, mouse; MIA; maternal immune activation; MLI;
920 Molecular layer interneuron; NES, Normalized Enrichment Score N, normoxia; ns, non-
921 significant; PC, Purkinje cell; PLI, Purkinje Layer Interneuron; Sal, saline; WM, white matter.
922
923

Figure 4

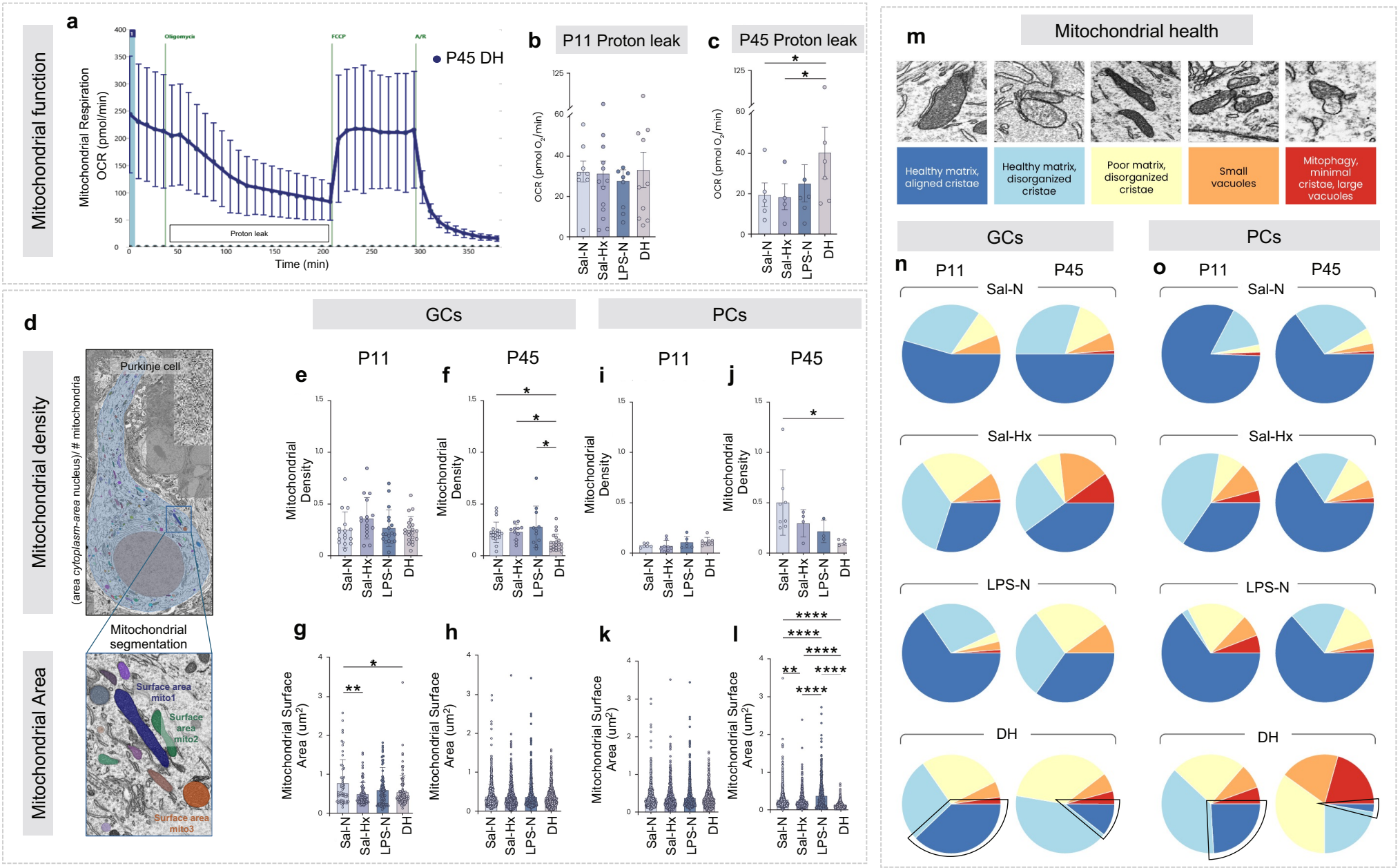
Mitochondrial function
a
Mitochondrial Respiration OCR (pmol/min)
Time (min)
Oligomycin
FCCP
A/R
Proton leak
P45 DH
b
P11 Proton leak
c
P45 Proton leak
OCR (pmol O2/min)
Sal-N
Sal-Hx
LPS-N
DH
d
Mitochondrial density
(area cytoplasm-area nucleus)/ # mitochondria
Purkinje cell
Mitochondrial segmentation
Mitochondrial Area
Surface area mito1
Surface area mito2
Surface area mito3
GCs
PCs
P11
P45
e
f
i
j
Mitochondrial Density
g
h
k
l
Mitochondrial Surface Area (um2)
m
Mitochondrial health
Healthy matrix, aligned cristae
Healthy matrix, disorganized cristae
Poor matrix, disorganized cristae
Small vacuoles
Mitophagy, minimal cristae, large vacuoles
n
o
Sal-N
Sal-Hx
LPS-N
DH

924 **Figure 4 - Neonatal Hx Exacerbates Mitochondrial Dysfunction Primed by MIA: a,**
925 Seahorse XF-derived graph output of metabolomic process in DH group at P45 showing the
926 oxygen consumption rate (y-axis) by time (x-axis) across metabolic phases. **b-c,** Bar graph
927 showing proton leak rates in mouse groups at postnatal days 11 (P11) and 45 (P45), as quantified
928 by Seahorse XF analysis. For **b**, n = 8-14 per group; one-way ANOVA with Tukey's multiple
929 comparisons. For **c**, n = 4-6 per group; ANOVA on ranks with pairwise comparisons, DH vs Sal-
930 Hx: *p = 0.0281; DH vs Sal-N: *p = 0.0484. **d**, Top image: schematic illustration from electron
931 microscopy of a PC with labelled mitochondria (colored); bottom image: example of magnified
932 illustration of three mitochondria (dark blue, green, orange) displaying the associated
933 mitochondria surface area. **e-f,** Quantification of mitochondrial density (number of mitochondria
934 per millimeter of GC) in GCs at P11 and P45 for each treatment group. For **e,** n = 16-21 per
935 group, Kruskal-Wallis test with Dunn's multiple comparisons test. For **f**, n = 11-21 per group,
936 Kruskal-Wallis test with Dunn's multiple comparisons test, Sal-N vs DH: *p = 0.012; LPS-N vs
937 DH: *p = 0.0168; DH vs Sal-Hx: *p = 0.0104. **g-h,** Quantification of mitochondrial surface area
938 in GCs at P11 and P45 for each treatment group. For **g**, n= 57-114 per group; one-way ANOVA
939 with Tukey's multiple comparisons test, Sal-N vs DH: *p = 0.0227; Sal-N vs Sal-Hx: **p =
940 0.003. For **h**, n = 669-757 per group, one-way ANOVA with Tukey's multiple comparisons test.
941 **i-j,** Quantification of mitochondrial density (number of mitochondria per millimeter of PC) in
942 PCs at P11 and P45 for each treatment group. For **i**, n = 6-8 per group, Kruskal-Wallis test with
943 Dunn's multiple comparisons test. For **j**, n = 3-5 per group; one-way ANOVA with Tukey's
944 multiple comparisons test, Sal-N vs Sal-Hx: *p = .0087. **k-l**, Quantification of mitochondrial
945 surface area in PCs at P11 and P45 for each treatment group. For **k**, n = 669-757 per group, one-
946 way ANOVA with Tukey's multiple comparisons test. For **l,** n = 528-1783 per group, one-way

947 ANOVA with Tukey's multiple comparisons test, $^{**}p = 0.0087$, $^{****}p < 0.0001$. **m**,
948 Representative EM images displaying mitochondrial quality assessment with a severity scoring
949 from 1 (least severe, blue) to 5 (most severe, red). **n-o,** Qualitative quantification of
950 mitochondrial health in both GCs and PCs for each mouse group shown as pie charts. Pie charts
951 *n*-values in Supplemental File 7. For **b-l**, data are represented as mean ± s.d.; statistics in
952 Supplemental File 7b-l. DH, double-hit; EM, electron microscopy; GC, granule cells; Hx,
953 hypoxia; LPS, lipopolysaccharide; N, normoxia; PC, Purkinje cells; Sal, saline.
954
955
956
957
958
959
960
961
962
963
964

Figure 5

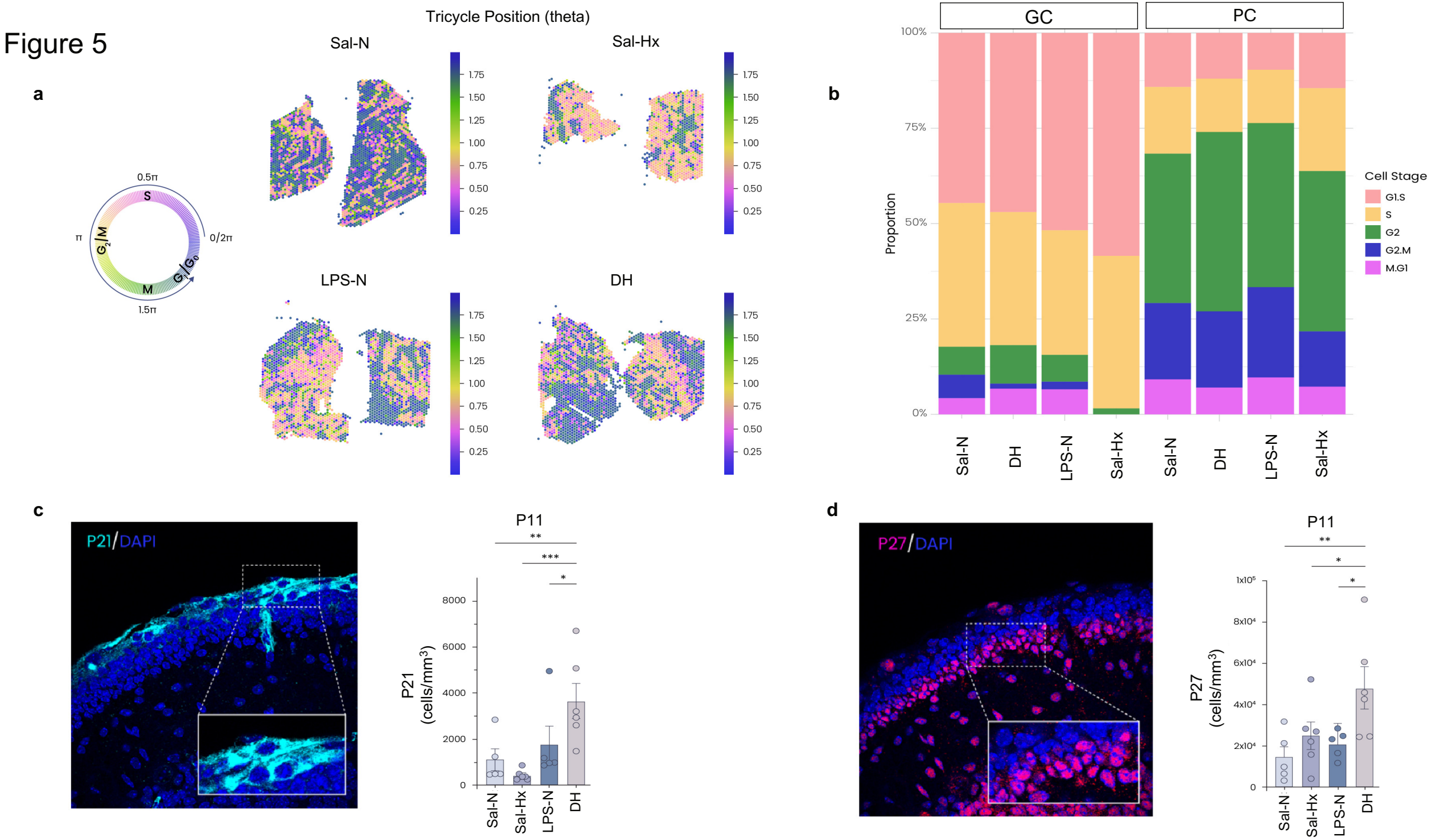
a
Tricycle Position (theta)
Sal-N
Sal-Hx
LPS-N
DH
0.5π
0/2π
π
1.5π
S
G2/M
M
G1/G0
1.75
1.50
1.25
1.00
0.75
0.50
0.25
b
GC
PC
100%
75%
50%
25%
0%
Proportion
Sal-N
DH
LPS-N
Sal-Hx
Sal-N
DH
LPS-N
Sal-Hx
Cell Stage
G1.S
S
G2
G2.M
M.G1
c
P21/DAPI
P11
**
***
*
P21 (cells/mm3)
8000
6000
4000
2000
0
Sal-N
Sal-Hx
LPS-N
DH
d
P27/DAPI
P11
**
*
*
P27 (cells/mm3)
1x10^5
8x10^4
6x10^4
4x10^4
2x10^4
0
Sal-N
Sal-Hx
LPS-N
DH

965 **Figure 5 - MIA Differentially Modulates Hx-induced Alterations in Neuronal Cell Cycle**
966 **Dynamics: a,** Left panel, schematic illustration of the cell cycle phases associated with the theta
967 value with color scale. Right panel, representative images of mouse cerebellar tissue for each
968 mouse group with spatial cell cycle distribution, corresponding to cell cycle phases based on
969 color legend. Colored scale matches approximately the cell cycle position variable (theta), <0.25
970 and >.1.75 (blue/purple) G_1/G_0 phase, 0.5 to 1 (pink to yellow) S phase, and 1.25 to 1.75 G_2/M
971 phase (green). **b**, Bar graph displaying the proportion in percentage (y-axis) of GCs and PCs in
972 different phases of the cell cycle in each mouse group (x-axis). Different colors correspond to
973 different cell cycles. **c**, Left image, representative image of immunofluorescent staining of p21
974 and DAPI in mouse tissue at 60x magnification. Right image, bar graph of p21 expression
975 calculated as cell per millimeter cube. **d**, Left image, representative image of immunofluorescent
976 staining of p27 and DAPI in mouse tissue at 60x magnification. Right image, bar graph of p27
977 expression calculated as cell per millimeter cube. For **c** and **d**, n = 5-6 per group; one-way
978 ordinary ANOVA with uncorrected Fisher's LSD; * $p < 0.05$, ** $p < 0.005$, *** $p = 0.0008$.
979 Data are represented as mean ± s.d. GC, granule cell; Hx, hypoxia; LPS, lipopolysaccharide;
980 LSD, least significant difference; N, normoxia; PC, Purkinje cell; Sal, saline.
981
982
983
984
985

Figure 6

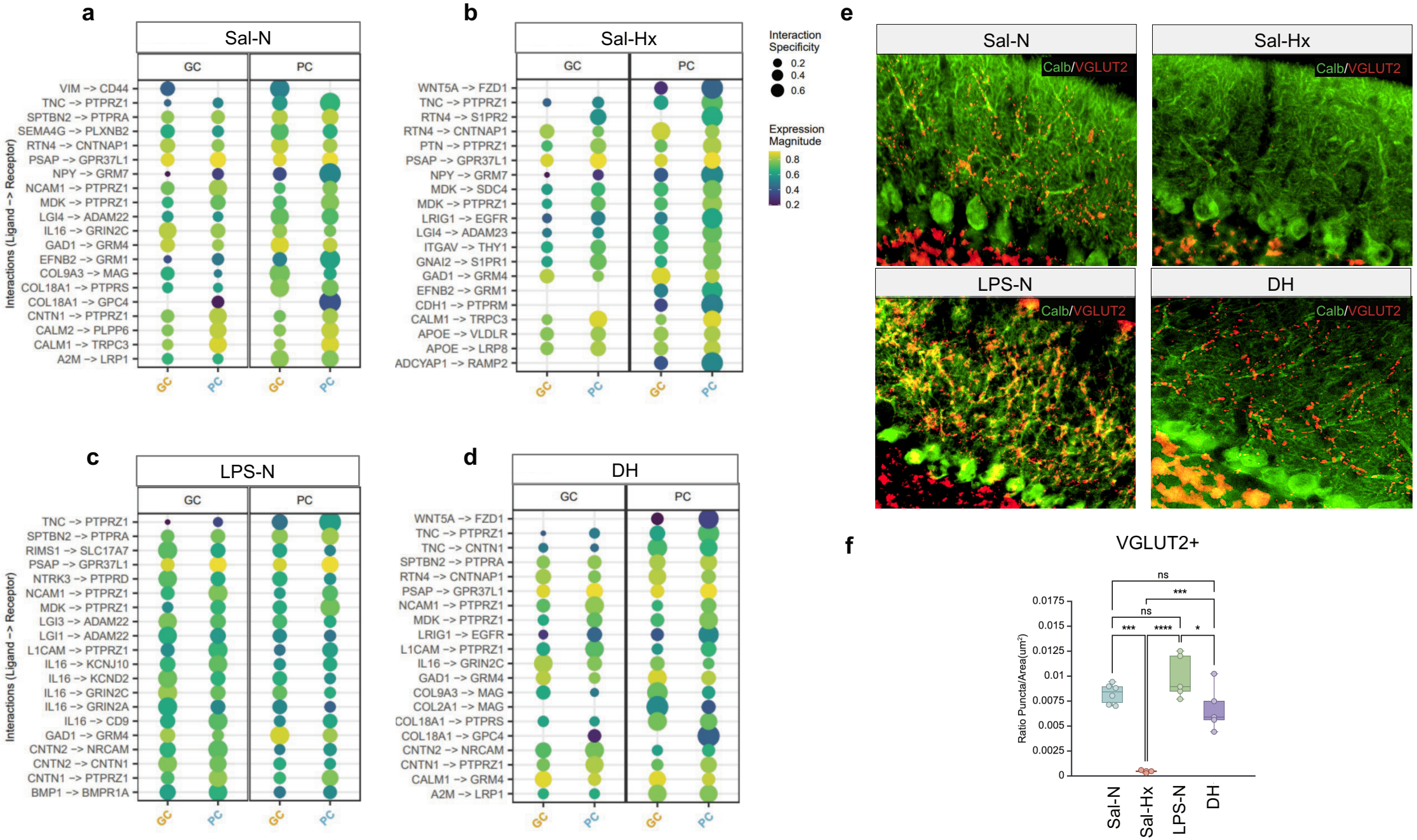
a
Sal-N
GC
PC
Interactions (Ligand -> Receptor)
VIM -> CD44
TNC -> PTPRZ1
SPTBN2 -> PTPRA
SEMA4G -> PLXNB2
RTN4 -> CNTNAP1
PSAP -> GPR37L1
NPY -> GRM7
NCAM1 -> PTPRZ1
MDK -> PTPRZ1
LGI4 -> ADAM22
IL16 -> GRIN2C
GAD1 -> GRM4
EFNB2 -> GRM1
COL9A3 -> MAG
COL18A1 -> PTPRS
COL18A1 -> GPC4
CNTN1 -> PTPRZ1
CALM2 -> PLPP6
CALM1 -> TRPC3
A2M -> LRP1
b
Sal-Hx
WNT5A -> FZD1
TNC -> PTPRZ1
RTN4 -> S1PR2
RTN4 -> CNTNAP1
PTN -> PTPRZ1
PSAP -> GPR37L1
NPY -> GRM7
MDK -> SDC4
MDK -> PTPRZ1
LRIG1 -> EGFR
LGI4 -> ADAM23
ITGAV -> THY1
GNAI2 -> S1PR1
GAD1 -> GRM4
EFNB2 -> GRM1
CDH1 -> PTPRM
CALM1 -> TRPC3
APOE -> VLDLR
APOE -> LRP8
ADCYAP1 -> RAMP2
Interaction Specificity
0.2
0.4
0.6
Expression Magnitude
0.8
0.6
0.4
0.2
c
LPS-N
TNC -> PTPRZ1
SPTBN2 -> PTPRA
RIMS1 -> SLC17A7
PSAP -> GPR37L1
NTRK3 -> PTPRD
NCAM1 -> PTPRZ1
MDK -> PTPRZ1
LGI3 -> ADAM22
LGI1 -> ADAM22
L1CAM -> PTPRZ1
IL16 -> KCNJ10
IL16 -> KCND2
IL16 -> GRIN2C
IL16 -> GRIN2A
IL16 -> CD9
GAD1 -> GRM4
CNTN2 -> NRCAM
CNTN2 -> CNTN1
CNTN1 -> PTPRZ1
BMP1 -> BMPR1A
d
DH
WNT5A -> FZD1
TNC -> PTPRZ1
TNC -> CNTN1
SPTBN2 -> PTPRA
RTN4 -> CNTNAP1
PSAP -> GPR37L1
NCAM1 -> PTPRZ1
MDK -> PTPRZ1
LRIG1 -> EGFR
L1CAM -> PTPRZ1
IL16 -> GRIN2C
GAD1 -> GRM4
COL9A3 -> MAG
COL2A1 -> MAG
COL18A1 -> PTPRS
COL18A1 -> GPC4
CNTN2 -> NRCAM
CNTN1 -> PTPRZ1
CALM1 -> GRM4
A2M -> LRP1
e
Sal-N
Calb/VGLUT2
Sal-Hx
Calb/VGLUT2
LPS-N
Calb/VGLUT2
DH
Calb/VGLUT2
f
VGLUT2+
Ratio Puncta/Area(um²)
0.0175
0.015
0.0125
0.01
0.0075
0.005
0.0025
0
ns
***
ns
***
****
*
Sal-N
Sal-Hx
LPS-N
DH

986 **Figure 6 - Perinatal Insults Rewire the Cerebellar Connectome through Divergent**
987 **Disruption of Cell–Cell Signaling Networks: a-d**, LIANA plots for each experimental group
988 displaying the specificity and expression magnitude of top 20 ligand-receptor interactions
989 between GC-GC, GC-PC and PC-PC, PC-GC. Interaction specificity scale going from 0.2 (small
990 circle) to 0.6 (big circle). Expression magnitude scale going from 0.2 (low, blue) to 0.8 (high,
991 yellow). Dashed line boxes indicate predicted interactions related to glutamatergic signaling and
992 synaptic transmission. **e**, Representative images of stained cerebellar tissue at 40x magnification
993 displaying in green (calbindin/Calb) PC and dendrites and in red (VGLUT2) excitatory synapse
994 puncta. **f**, Graph displaying the ratio of number of excitatory puncta divided by area
995 (number/mm^2). Ordinary one-way ANOVA with Tukey's multiple comparisons test; n=4-5 per
996 mouse group; *$p < 0.05$, **$p < 0.005$, ***$p < 0.0005$. Data are represented as mean ± s.d. GC,
997 granule cell; Hx, hypoxia; LPS, Lipopolysaccharide; N, normoxia; PC, Purkinje cell; Sal, saline.
998
999
1000
1001
1002
1003
1004

Figure 7

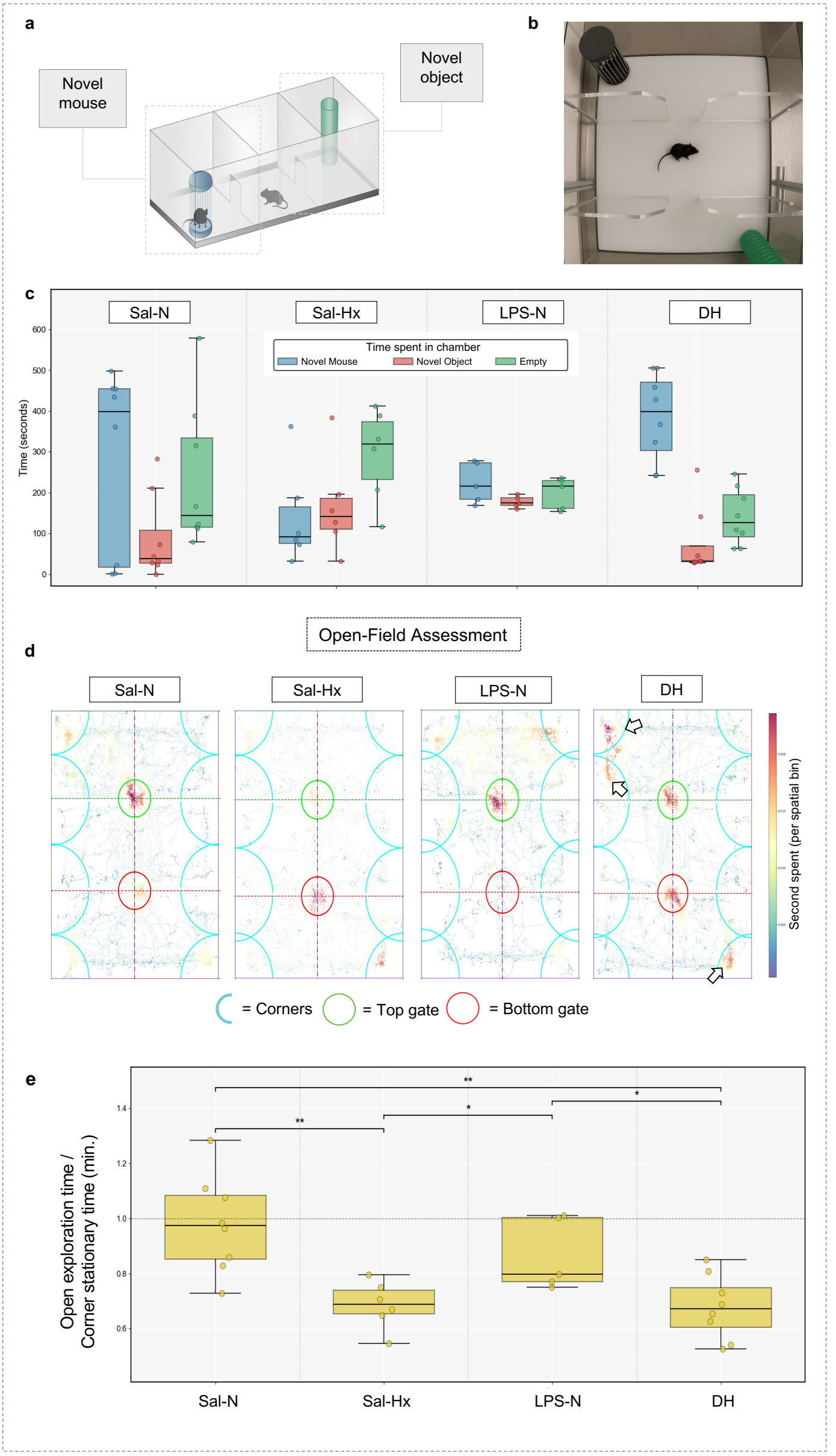
a
Novel mouse
Novel object
b
c
Sal-N
Sal-Hx
LPS-N
DH
Time spent in chamber
Novel Mouse
Novel Object
Empty
Time (seconds)
0
100
200
300
400
500
600
Open-Field Assessment
d
Sal-N
Sal-Hx
LPS-N
DH
Second spent (per spatial bin)
= Corners
= Top gate
= Bottom gate
e
Open exploration time / Corner stationary time (min.)
0.6
0.8
1.0
1.2
1.4
**
*
**
*
Sal-N
Sal-Hx
LPS-N
DH

1005 **Figure 7 - MIA Modifies the Neurobehavioral Impact of Neonatal Hx: a**, Schematic
1006 illustration of the modified apparatus for three-chambered social assay, which evaluates general
1007 sociability tendencies in mice. On the left, the novel mouse chamber displaying an unfamiliar
1008 mouse in a cylindric cage; in the middle chamber, illustration representing the test subject
1009 mouse; on the right, cylindric novel object in green. **b,** Illustration reproducing the experimental
1010 setup created utilizing a photograph of the original setup. **c**, Graph displaying amount of time
1011 spent in chamber (y-axis) for each treatment group. n = 6-8 per group. ***p <.001; between
1012 groups: one-way ANOVA with independent samples t-test (Welch's test); within groups:
1013 independent samples t-test. Blue boxplot represents time spent in the chamber containing the
1014 novel mouse. Red boxplot represents time spent in chamber containing the novel object. Green
1015 boxplot represents time spent in any other area within the full arena (exploring). Data are
1016 displayed as mean ± S.E.M. **d**, Sample traces of tracked movement from individual mice
1017 representative of each experimental group during the three-chamber open field assessment.
1018 Images show traces of movement between the three chambers, with the chamber corner
1019 delimited by the semi-circle (light blue), the top gate area (green) and the bottom gate area (red).
1020 Horizontal red and green line mark chambers' boundaries, vertical purple line represents
1021 chamber midline. Heatmap scale represents second spent per spatial bin going from 0.01s (blue)
1022 to 0.06s (red). **e**, Boxplot graph representing the [open exploration time / corner and gate
1023 stationary time] ratio across experimental groups in the open field test. Horizontal dashed line
1024 indicates balanced ratio (ratio =1). Statistical analysis was performed using One-way ANOVA
1025 with Tukey's multiple comparison test. Data are presented as mean ± s.d. *p < .05, ** p< .01.
1026 Hx, hypoxia; LPS, lipopolysaccharide; N, normoxia; Sal, saline.
1027

Figure 8

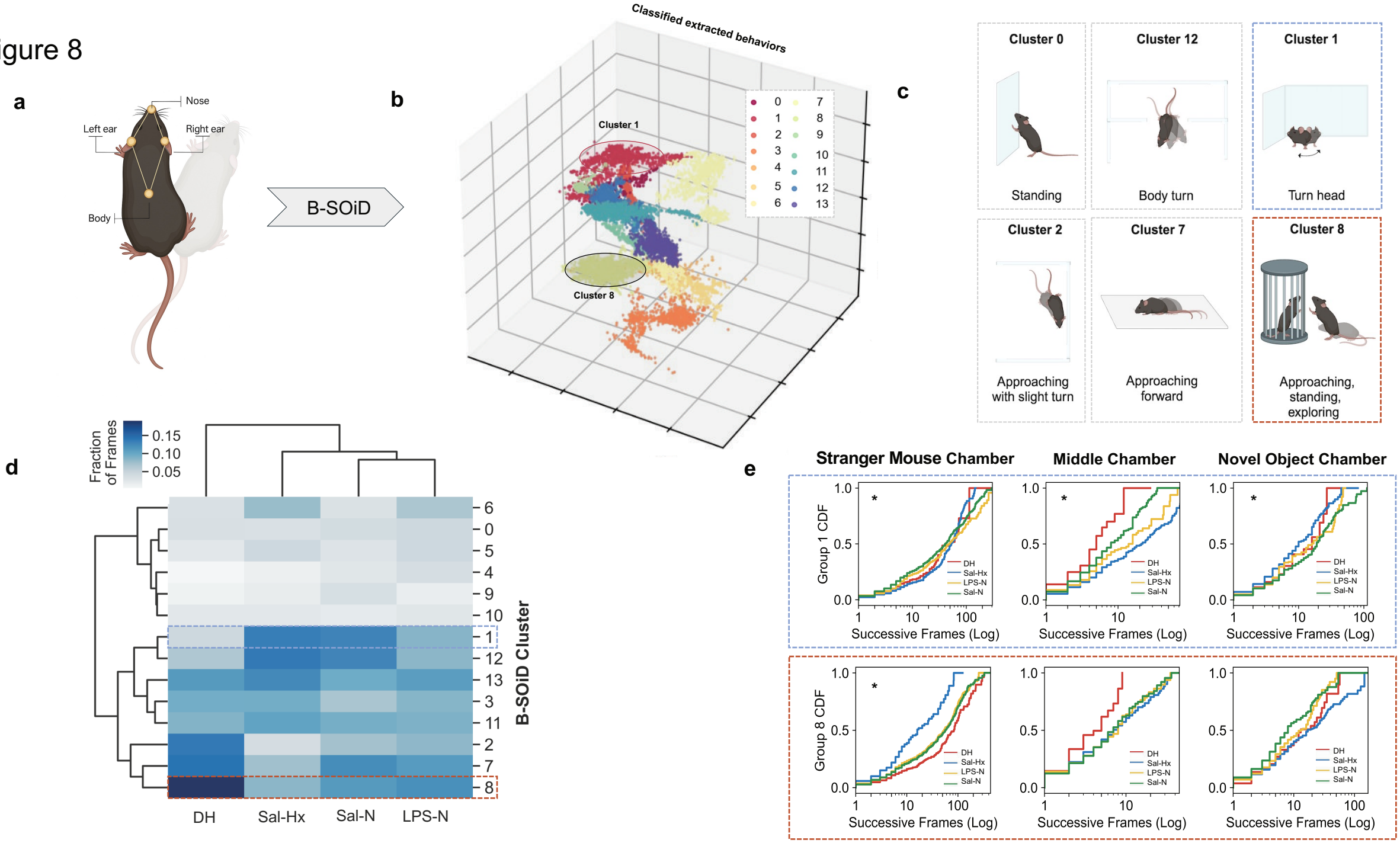
a
Nose
Left ear
Right ear
Body
B-SOiD
b
Classified extracted behaviors
Cluster 1
Cluster 8
0
1
2
3
4
5
6
7
8
9
10
11
12
13
c
Cluster 0
Standing
Cluster 12
Body turn
Cluster 1
Turn head
Cluster 2
Approaching with slight turn
Cluster 7
Approaching forward
Cluster 8
Approaching, standing, exploring
d
Fraction of Frames
0.15
0.10
0.05
B-SOiD Cluster
DH
Sal-Hx
Sal-N
LPS-N
e
Stranger Mouse Chamber
Middle Chamber
Novel Object Chamber
Group 1 CDF
Group 8 CDF
Successive Frames (Log)
DH
Sal-Hx
LPS-N
Sal-N

1028 **Figure 8 - MIA Pre-Exposure Shifts Hx-Induced Motor Stereotypies Toward Heightened**
1029 **Social Behavior: a**, Schematic illustration of an experimental mouse and the corresponding
1030 body points utilized to track mouse movement. **b**, 3D-graph displaying the 14 kinematic
1031 behavioral clusters – groups comprised of same kinematic motifs (fraction of video representing
1032 a specific movement) - identified by the B-SOiD algorithm. B-SOiD is an unsupervised
1033 machine-learning tool that classifies high-resolution kinematics into distinct behavioral patterns.
1034 **c**, Illustrations examples displaying the kinematic motifs associated with the corresponding
1035 cluster. **d**, Heatmap depicting the kinematic motifs frequency assessed as fraction of frames with
1036 B-SOiD for the identified 14 kinematic clusters in each of the groups. Dark blue indicates a
1037 higher fraction of frames; light blue indicates a lower fraction of frames. Brackets show group
1038 structure/pairings for statistical comparisons included in Results section. n = 3-10 per group. **e**,
1039 Graphs showing the duration as Cumulative Distribution Function (CDF, y-axis) of kinematic
1040 cluster 1 (top) and 8 (bottom) for all groups in each of the three chambers calculated as
1041 successive frames log (x-axis). group. Wasserstein distance with Benjamini-Hochberg correction
1042 applied to p-values. *indicates graph with at least one significant different interaction; statistics
1043 in Supplemental File. For **d-e**, n = 3-10 per group. DH, double-hit; LPS, lipopolysaccharide; Hx,
1044 hypoxia; N, normoxia; Sal, saline.
1045
1046
1047
1048

Extended Data Figure 1

a

Two-way RM ANOVA	SS	DF	MS	F (DFn, DFd)	P value
Sessions x Condition	1696435	49	34621	F (49, 336) = 4.444	P<0.0001
Sessions	1245464	7	177923	F (7, 336) = 22.84	P<0.0001
Condition	1374825	7	196404	F (7, 48) = 11.54	P<0.0001
Subject	817223	48	17025	F (48, 336) = 2.185	P<0.0001
Residual	2617723	336	7791		

#	Tukey's multiple comparisons test	Predicted (LS) mean diff.	95.00% CIs	Summary	Adjusted P Value
5	Sal-N Post-perturbation vs. DH Post-perturbation	-366.1	-514.9 to -217.2	****	<0.0001
5	Sal-N Post-perturbation vs. LPS-N Post-perturbation	-219.8	-368.6 to -70.90	***	0.0002
5	Sal-N Post-perturbation vs. Sal-Hx Post-perturbation	-186.6	-335.4 to -37.71	**	0.0038

Post-perturbation step-time

b

Two-way RM ANOVA	SS	DF	MS	F (DFn, DFd)	P value
Sessions x Condition	623.3	21	29.68	F (21, 168) = 1.694	P=0.0359
Sessions	878.3	7	125.5	F (7, 168) = 7.161	P<0.0001
Condition	283.5	3	94.49	F (3, 24) = 0.9169	P=0.4476
Subject	2473	24	103.1	F (24, 168) = 5.881	P<0.0001
Residual	2944	168	17.52		

#	Tukey's multiple comparisons test	Predicted (LS) mean diff.	95.00% CIs	Summary	Adjusted P Value
5	Sal-N vs. Sal-Hx	-10.03	-17.13 to -2.916	**	0.0019
5	LPS-N vs. Sal-Hx	-11.92	-19.87 to -3.970	***	0.0008
5	Sal-Hx vs. DH	11.22	3.269 to 19.16	**	0.0019

Missteps

1049

1050 **Extended Data Fig. 1: a** and **b,** Tables displaying the significant statistical results of two-way
1051 Repeated Measure (RM) ANOVAs with Tukey's multiple comparisons test for between
1052 experimental group comparison following ErasmusLadder testing. Top tables display ANOVA
1053 statistics followed by between-group comparisons in post-perturbation step time (**a**) and missteps
1054 (**b**). #, ErasmusLadder session number; CI, confidence intervals; DF, degrees of freedom; LS,
1055 least squares; MS, mean square; SS, sum of squares.

1056

1057

1058

1059

1060

1061

1062

1063

1064

1065

1066

1067

1068

1069

1070

Extended Data Figure 2-1

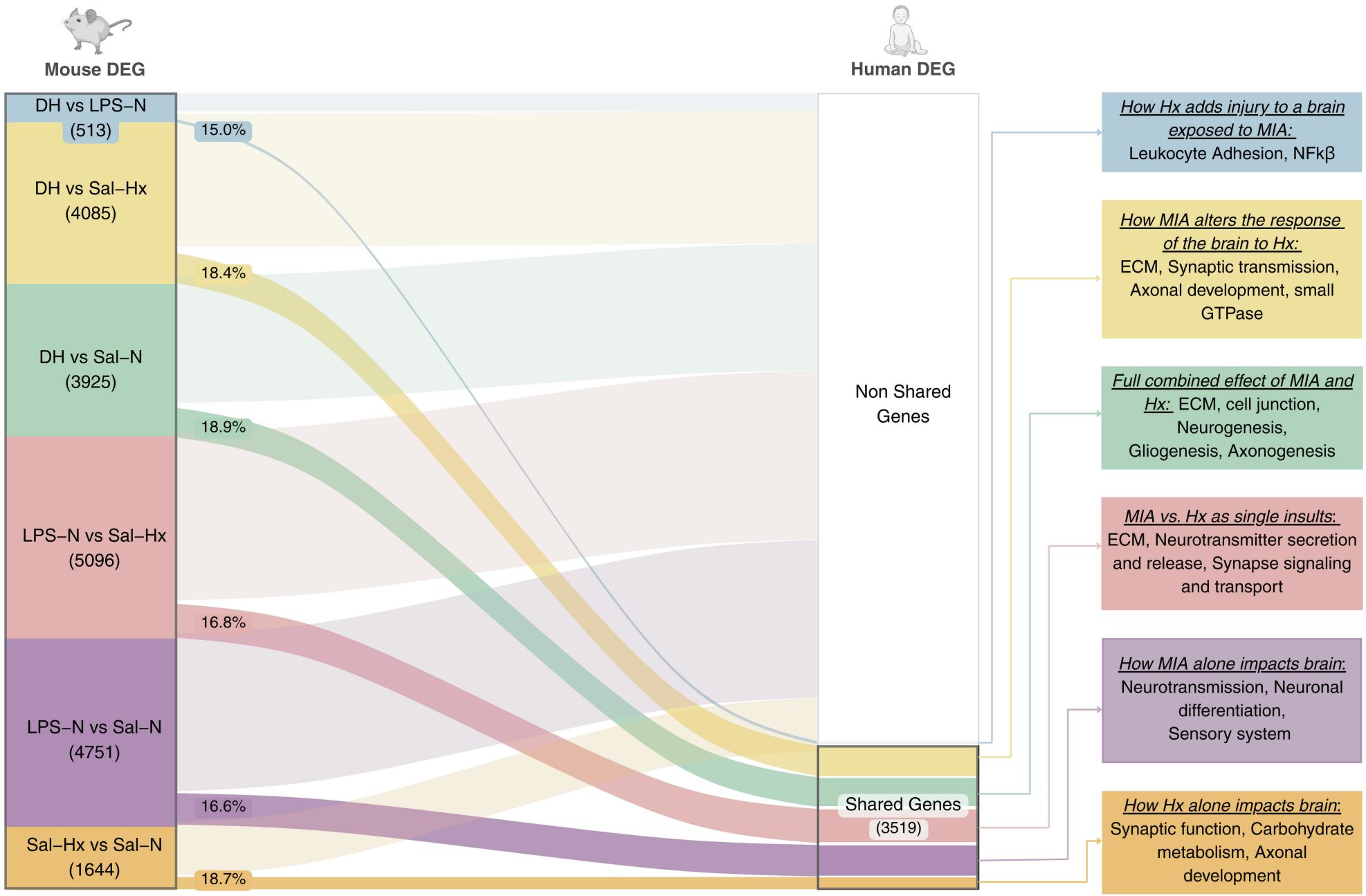

1071 **Extended Data Fig. 2-1: a,** On the right, diagram illustrating the shared (color-coded) vs. non-
1072 shared (transparent) genes (p-value < 0.05) identified in DH mouse model comparisons between
1073 experimental groups at P45 and human post-mortem cerebellar tissues human (Preterm vs Term).
1074 Number below the label identify the number of identified genes, and percentage correspond to the
1075 percentage of genes shared. On the left, color-coded boxes displaying top significantly GO-derived
1076 enriched biological processes associated with each shared genes comparisons (color-coded; $p <$
1077 0.05). $n = 4$ per human group, $n = 7$ per mouse group. DEG, differentially expressed genes; DH,
1078 double-hit; ECM, extracellular matrix; GO, gene ontology; GTP, Guanosine Triphosphate; Hx,
1079 hypoxia; LPS, lipopolysaccharide; N, normoxia; NFkb, Nuclear Factor kappa-light-chain-
1080 enhancer of activated B cells; Sal, saline.
1081
1082
1083
1084
1085
1086
1087
1088
1089
1090
1091
1092

Extended Data Figure 2-2

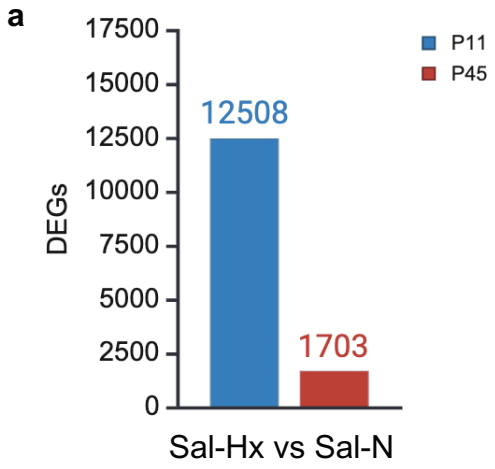

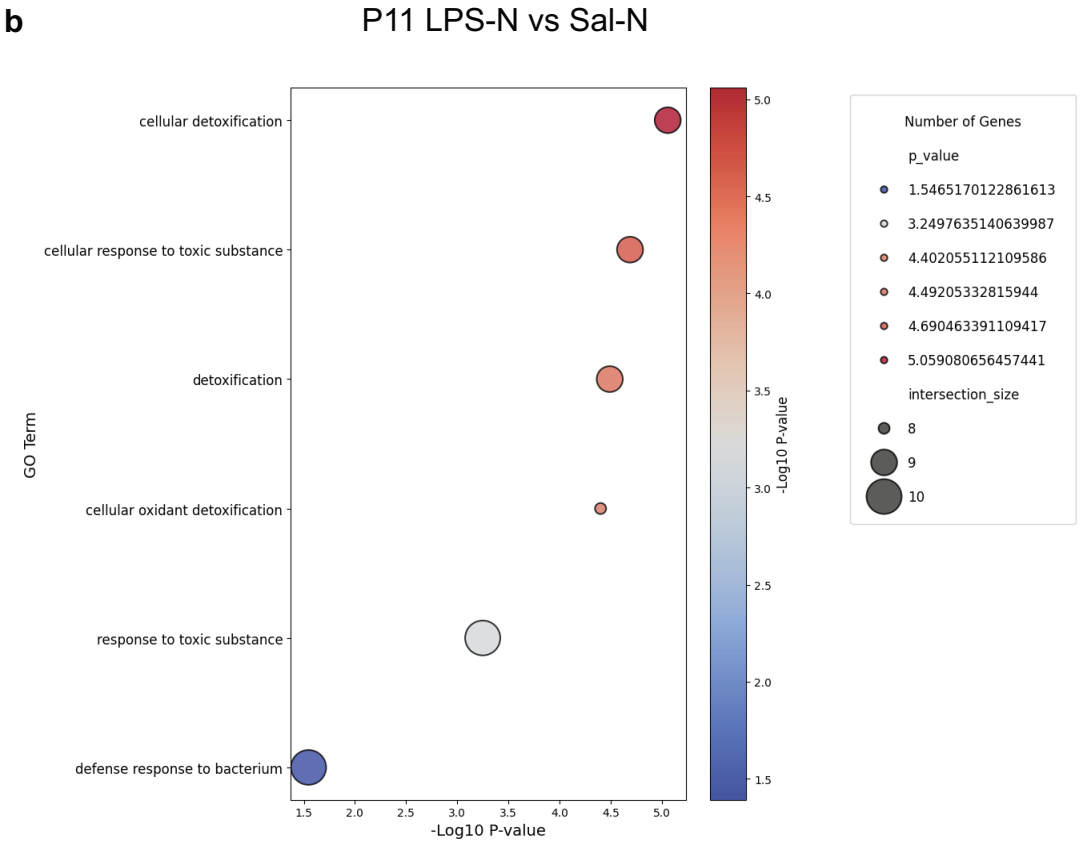

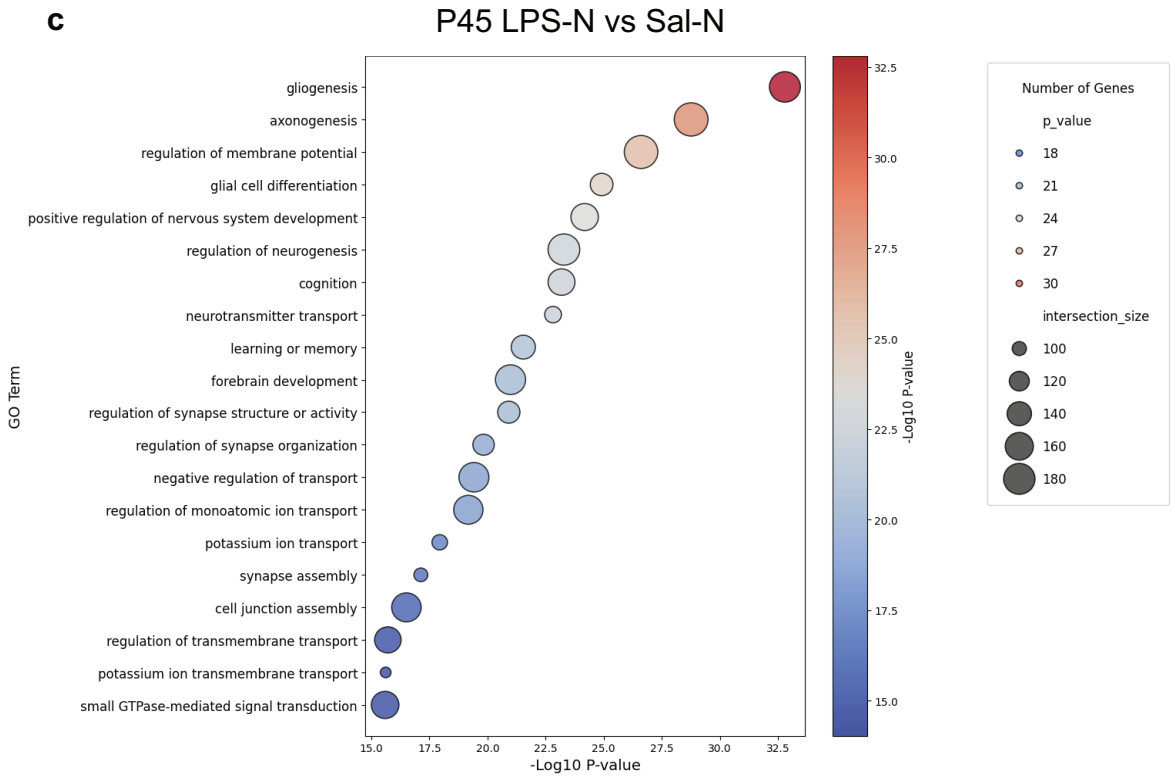

1093 **Extended Data Fig. 2-2: a-c**, Bar graphs display the number of significant DEGs (y-axis, *p*-value
1094 < 0.05) identified in pairwise experimental comparisons at two developmental stages (P11 – blue
1095 and P45 – red). Number of top of the bars represent exact number of DEGs. Comparisons: Sal-Hx
1096 and Sal-N. **b-c**, Bubble plots displaying the top 20 significantly enriched biological process terms
1097 identified via GO enrichment analysis for selected experimental comparisons. Bubble size
1098 corresponds to the number of genes in each GO term, while the color gradient represents
1099 significance level (-log10 adjusted p-value), with red indicating highly significant enrichment and
1100 blue representing lower significance. Comparison: LPS-N and Sal-N groups. **b**, P11; **c**, P45. For
1101 **a-c**, *n* = 2/5 per group. DEG, differentially expressed genes; DH, double-hit; GO, gene ontology;
1102 Hx, hypoxia; LPS, lipopolysaccharide; N, normoxia; Sal, saline.
1103
1104
1105
1106
1107
1108
1109
1110
1111
1112
1113
1114

Extended Data Figure 2-3

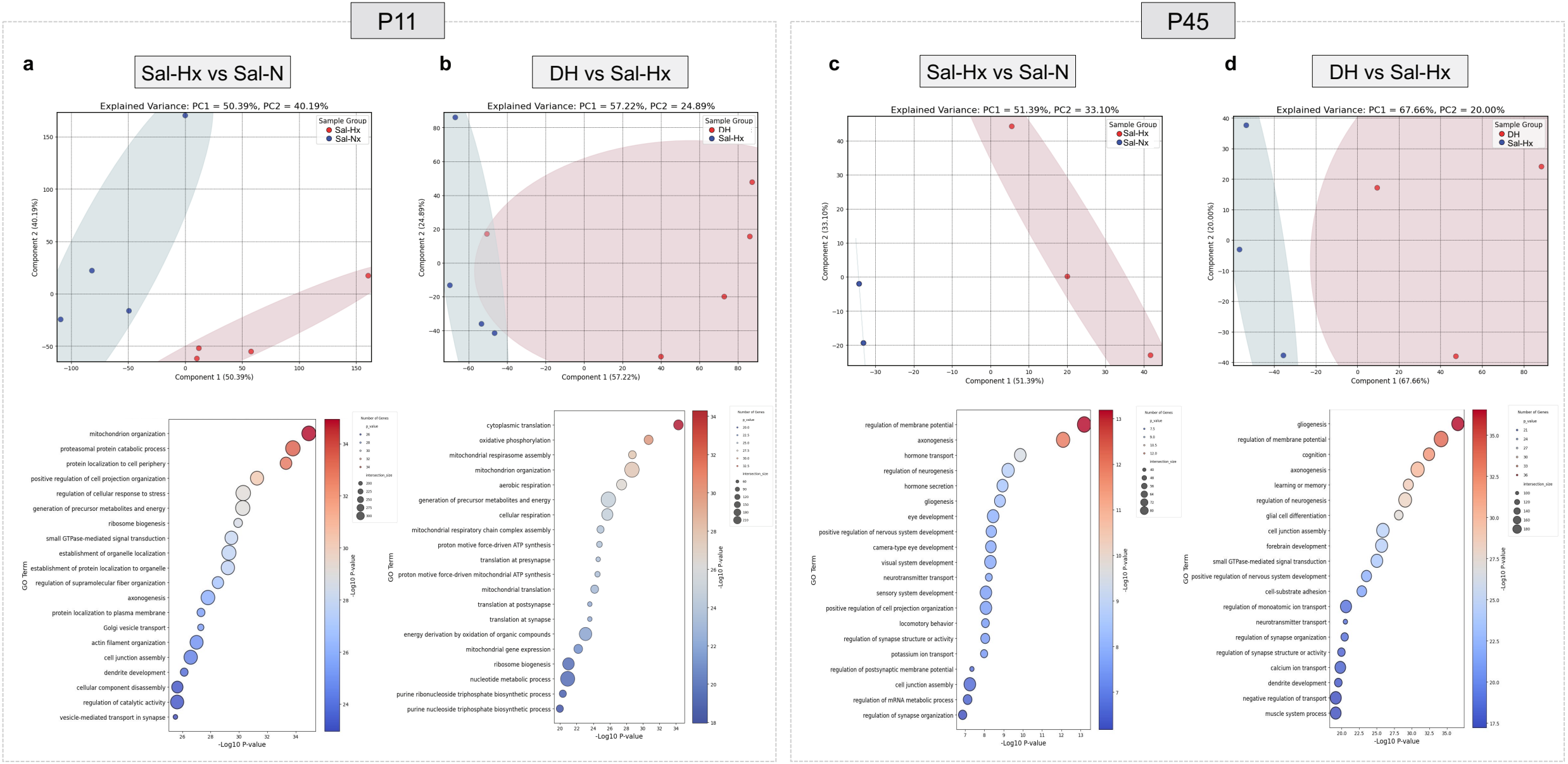

1115 **Extended Data Fig. 2-3: a-b**, Top image, PCA plot comparison between **a**, Sal-Hx and Sal-N; **b**,
1116 DH and Sal-Hx at P11. PCA scatter plot demonstrates distinct separation between groups along
1117 the first two principal components (**a**, PC1=50.93%, PC2=40.19%, total variance explained:
1118 91.12%; **b**, PC1=57.22%, PC2=24.89%, total variance explained: 82.11%). *n*=4 per group. **c-d**,
1119 Top image, PCA plot comparison between **c**, Sal-Hx and Sal-N; **d**, DH and Sal-Hx at P45. PCA
1120 scatter plot demonstrates distinct separation between groups along the first two principal
1121 components (**a**, PC1=51.39%, PC2=33.10%, total variance explained: 84.49%; **b**, PC1=67.66%,
1122 PC2=20%, total variance explained: 87.66%). *n*=2/3 per group. **a-d**, PCA colored ellipses
1123 represent 95% confidence intervals. Bottom image, corresponding GO enrichment bubble plot
1124 displaying top significantly enriched biological processes associated with DEGs ($p < 0.05$). The
1125 bubble size reflects the number of genes within each GO term (small size – lower number of genes,
1126 big size – higher number of genes), color gradient and x-axis indicate significance (-log10 adjusted
1127 P-value; red indicates higher significance, blue indicates lower significance). DEG, differentially
1128 expressed genes; DH, double-hit; GO, gene ontology; Hx, hypoxia; LPS, lipopolysaccharide; N,
1129 normoxia PC/PCA, principal component analysis; Sal, saline.
1130
1131
1132
1133
1134
1135
1136
1137

Extended Data Figure 3

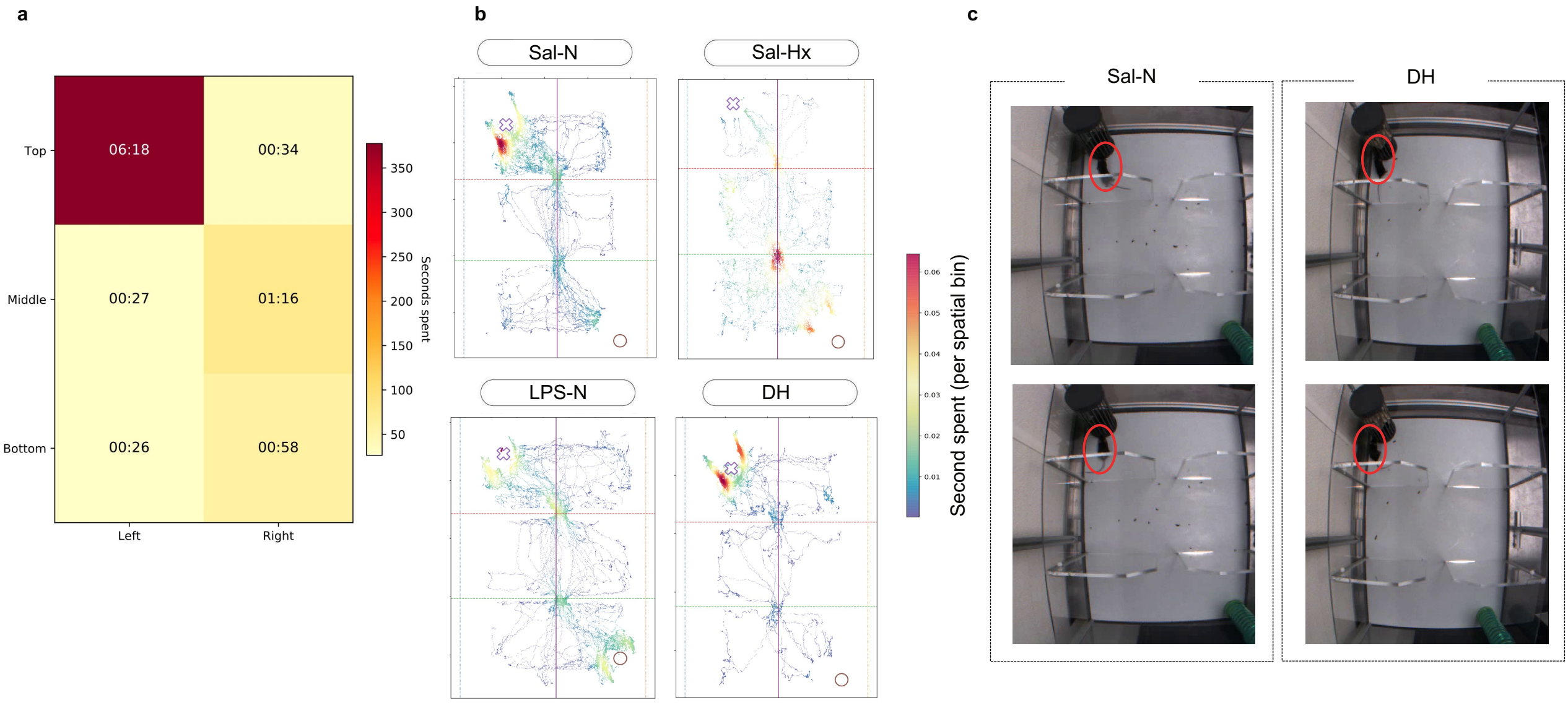

1138 **Extended Data Fig. 3: a**, Representative schematic of the six-grid time outcome. Color scale
1139 indicates second spent ranging from 50s (yellow) and 350s (red). **b**, Representative schematic of
1140 the three-chamber social movement tracking for each condition. Stranger mouse is marked with
1141 an x-symbol; novel object is marked with a circle-symbol. Dashed lines represent borders.
1142 Colored scale shows second spent per spatial bin ranging from 0.005s (blue) to 0.020 (red). **c**,
1143 Raw representative images of normoxic control or DH mice during the social test. Red circles
1144 indicate the testing mouse position in the chamber. DH, double-hit; Hx, hypoxia; LPS,
1145 lipopolysaccharide; N, normoxia
1146
1147
1148
1149
1150
1151
1152
1153
1154
1155
1156
1157
1158

Extended Data Figure 4-1

Cluster 0

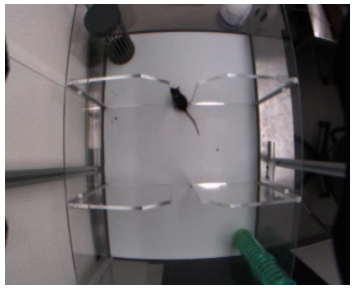

Cluster 1

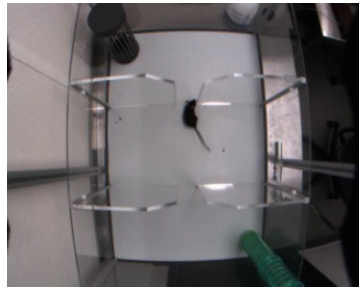

Cluster 2

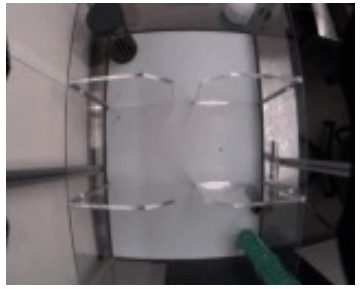

Cluster 3

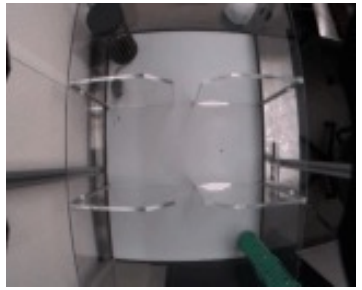

Cluster 4

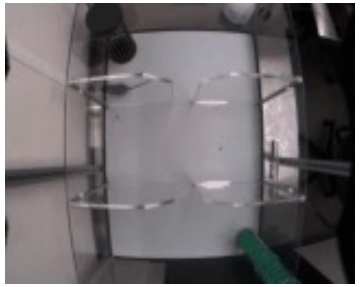

Cluster 5

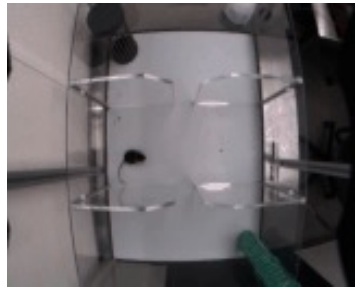

Cluster 6

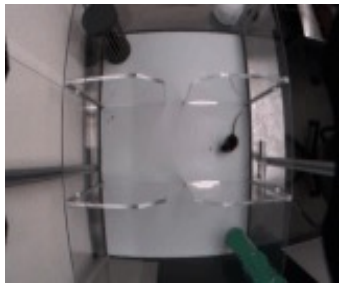

Cluster 7

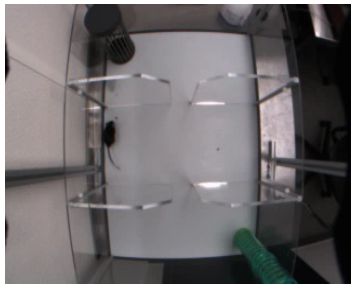

Cluster 8

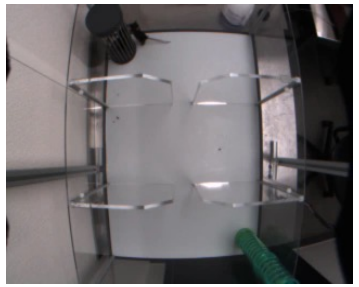

Cluster 9

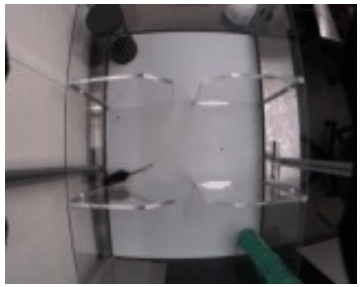

Cluster 10

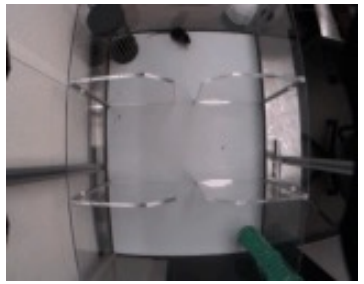

Cluster 11

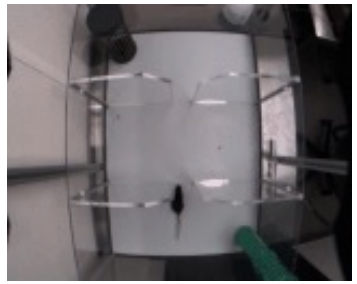

Cluster 12

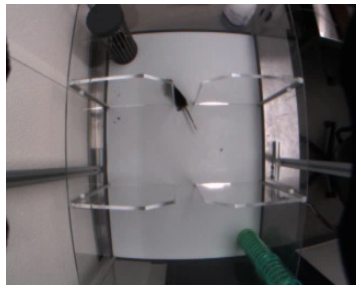

Cluster 13

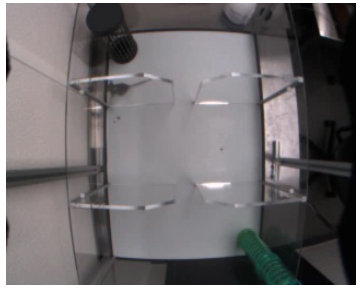

Extended Data Fig. 4-1: Representative video segments illustrating distinct kinematic clusters identified by B-SOiD. Each clip exemplifies a characteristic locomotor motif corresponding to a specific data-driven behavioral cluster extracted from high-resolution movement tracking.

Extended Data Figure 4-2

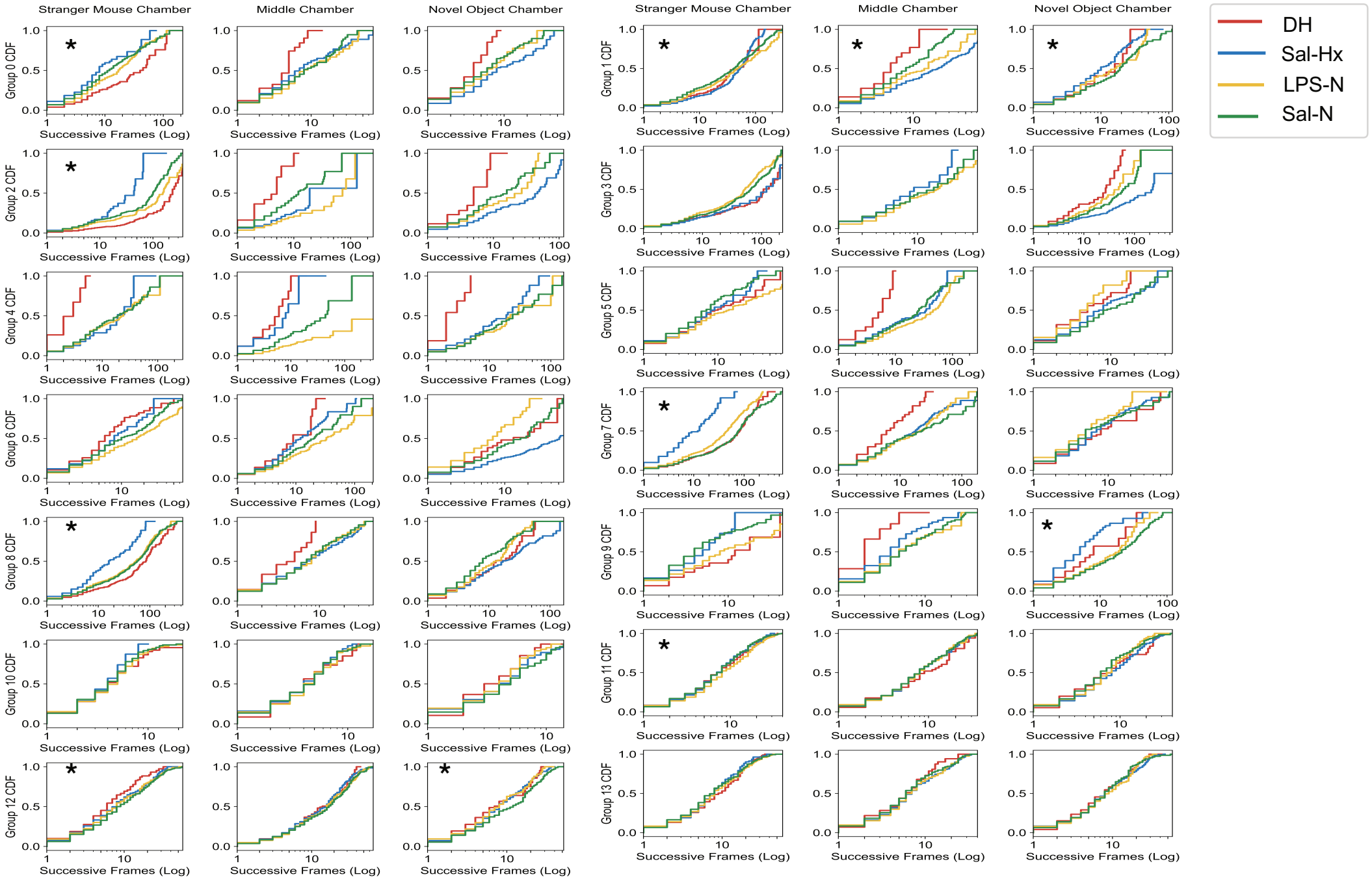

1181 **Extended Data Fig. 4-2:** Graphs showing the duration as Cumulative Distribution Function (CDF,
1182 y-axis) of each kinematic cluster for all groups in each of the three chambers calculated as
1183 successive frames log (x-axis). n = 3-10 per group. Wasserstein distance with Benjamini-Hochberg
1184 correction applied to p-values. *Indicates graph with at least one significant different interaction;
1185 statistics in Supplemental File. DH, double-hit; LPS, lipopolysaccharide; Hx, hypoxia; N,
1186 normoxia; Sal, saline.